CHAPTER -5

Low Cycle Fatigue Behaviour of Inconel 617 Alloy

5.1 Introduction

The combination of very high temperatures of operation and long duration of service requires materials with good thermal stability. The primary mode of failure of components in the high temperature applications is from cyclic loading (fatigue) resulting during start up and shut down operations. Temperature induced cyclic strains of different magnitude are caused by thermal stresses generated during such operations and thus understanding of the low cycle fatigue behaviour and related deformation mechanisms at room temperature as well as at elevated temperatures is necessary. Several investigators have studied low cycle fatigue behaviour of the Inconel 617 alloy as discussed in Chapter 1, Section 1.9. However, only limited investigations have been carried out on the comparative evaluation of fatigue properties, deformation and fracture behaviour at various temperatures such as RT, 750^{o}C and 850^{o}C. The deformation behaviour in conjunction with TEM studies is also not analysed in detail for cyclic loading at the above three temperature. In the present chapter, the effect of temperature and strain amplitude on LCF behaviour of Inconel 617 alloy are analysed in detail. Low cycle fatigue tests were conducted at RT, 750^{o}C and 850^{o}C in air, under fully reversed axial strain controlled mode at constant strain rate of $5x10^{-3}$ s^{-1} to determine the influence of temperature on low cycle fatigue (LCF), deformation and fracture behaviour. The behaviour of the alloy under cyclic loading is compared with the behaviour under monotonic loading as well. Detailed characterisation of deformation and fracture behaviour of samples tested at three temperatures was analysed and discussed. Interrupted tests were also carried out at room temperature to study the deformation behaviour of the alloy exhibiting cyclic softening and hardening.

5.2 Methodology

Cylindrical LCF specimens of Inconel 617 alloy in the solution annealed condition as per ASTM E 606 with gauge section of 5.5 mm diameter, 15 mm gauge length were prepared and tested at three temperatures, namely RT, 750°C and 850°C, at strain amplitudes ranging from ±0.20% to ±0.50% at a constant strain rate of $5x10^{-3}$ s^{-1}. The microstructural changes that occurred during testing were assessed by optical metallography of longitudinal and transverse sections of the tested specimens, close to fracture ends. Detailed microstructural characterization of the fracture and deformation behaviour was carried out using SEM and TEM respectively.

5.3 Tensile Behaviour at RT, 750^{o}C and 850^{o}C

Fig. 5.1 shows engineering strain-strain curves of Inconel 617 alloy at the three temperatures studied. It is obvious from the curves that typical behaviour of ductile material is observed for this alloy at all the three temperatures. Table 5.1 shows the tensile properties obtained from the tests conducted at a strain rate of $5x10^{-3}$ s^{-1}. Reduction in ultimate tensile strength was observed with increase in the temperature. Uniform elongation decreased with increase in temperature (Fig. 5.1). Similar results were observed by Mo et al. [37]. Degree of work hardening (S_{UTS}/S_{YS}) was more at 750^{o}C compared to that at RT. However, it showed decrement again at 850^{o}C. Work hardening parameters were derived using Ludwigson equation for the samples tested at RT and 750^{o}C and using Hollomon equation for the samples tested at 850^{o}C. The parameters derived are given in Table 5.2. The value of *K* and *n* found to decrease at 750^{o}C compared to RT. However, the values of *K* and *n* found to increase again at 850^{o}C.

Table 5.1: Tensile Properties of the Inconel 617 Alloy at Different Temperatures.

Temperature, ^{o}C	0.2% Y.S, MPa, (S_{YS})	U.T.S, MPa (S_{UTS})	Elongation % (e_{pf})	Uniform elongation % (e_{pu})	Degree of work hardening (S_{UTS}/S_{YS})
RT	372	785	73	55	2.11
750	180	435	71	36	2.41
850	189	240	63	7	1.45

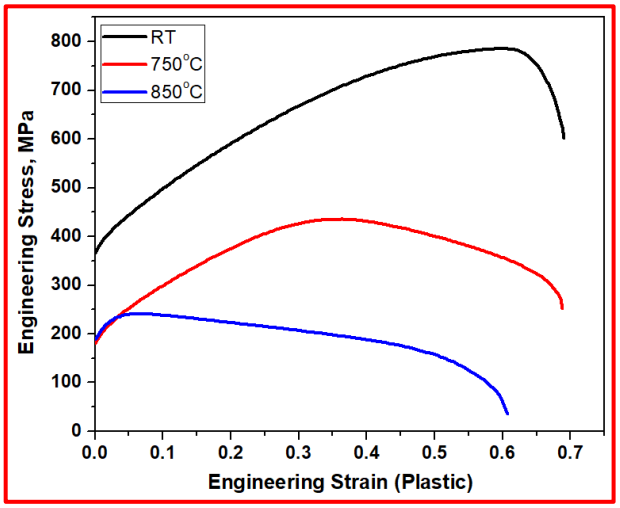

Fig. 5.1: Engineering stress- plastic strain curves of Inconel 617 alloy at different temperatures.

Table 5.2: Work Hardening Parameters Derived at Various Temperatures.

Temperature ^{o}C	Relationship used	K	n	K_1	$-n_1$
RT	Ludwigson	2095	0.6337	5.86	14.21
750	Ludwigson	1625	0.5943	5.45	13.93
850	Hollomon	1283	0.589	--	--

5.4 Low Cycle Fatigue Behaviour

Table 5.3 gives the fatigue data obtained from the LCF tests at three different temperatures RT, 750^{o}C and 850^{o}C respectively. It is evident from the table that the fatigue life was decreased with increase in the temperature and strain amplitude. At RT,

run out was observed at strain amplitude of ±0.18% i.e. no failure of the sample was noticed. At 750°C though decrease in life was observed with increase in strain amplitude the drop in life was drastic above ±0.375% strain amplitude, nearly similar trend was observed at 850°C corresponding to the same strain amplitudes. The number of cycles to macro crack initiation (N_i), number of cycles to failure (N_f), were derived using quotient curve method [57] and the ratio of N_i/N_f are given in the Table 5.3. Since the ratio of N_i/N_f was more than $\simeq$ 0.8 for all the LCF tests, the hysteresis loops corresponding to half-life ($0.5N_f$) for the evaluation of plastic strain amplitude and the cyclic stress range were not affected by macro crack initiation and propagation [57]. Hence the values of plastic strain amplitude ($\Delta\varepsilon_p/2$) and stress amplitude ($\Delta\sigma/2$) were taken from hysteresis loop of the cycle corresponding to half-life ($0.5N_f$) is justified.

Table 5.3: Low Cycle Fatigue (LCF) Data of Inconel 617 Alloy at Different Temperatures and Strain Amplitudes.

$\Delta\varepsilon_t/2$	N_i (Cycles)	N_f (Cycles)	N_i/N_f	$\Delta\varepsilon_p/2$	$\Delta\sigma/2$ (MPa)	$(\sigma_T)_{1/2}$ (MPa)	ΔH
Room Temperature							
0.0018	--	Run out*	---	0.00011	322	305	0.19
0.0020	92,011	95,931	0.96	0.00043	369	359	0.22
0.0025	30,966	35,329	0.88	0.00079	377	372	0.23
0.00375	12,039	13,239	0.91	0.00168	441	415	0.27
0.0042	6,250	6,994	0.89	0.00198	452	440	0.30
0.0050	5,593	5,743	0.97	0.00253	505	496	0.26
750°C							
0.0020	6,564	6,926	0.95	0.00051	286	274	1.05
0.0025	5,341	6,237	0.86	0.00054	319	309	1.19
0.00375	746	945	0.79	0.00120	454	443	1.16
0.0050	367	405	0.91	0.00219	531	514	0.98
850°C							
0.0020	2350	2600	0.90	0.00035	260	252	0.29
0.0025	1023	1190	0.85	0.00095	272	265	0.48
0.00375	820	973	0.84	0.00175	295	292	0.45
0.0050	390	435	0.89	0.00290	350	342	0.39
* Run out at 1,82,000; ΔH: Degree of hardening; σ_T : Tensile stress amplitude at half-life							

It is evident that the values of $\Delta\varepsilon_p/2$ increased with increase in strain amplitude as well as temperature. The stress amplitude also increased with increase in strain amplitude at all the three temperatures. At RT, the stress amplitude values were found to be higher than the values observed at 750^{o}C except at the higher strain amplitude (±0.50%) where the stress amplitude was higher than that observed at RT for the respective strain amplitude. The stress amplitude values at 850^{o}C were found to be lower than at the values at RT and 750^{o}C.

The variation of cyclic stress amplitude with number of cycles for different total strain amplitudes, also known as cyclic stress response, is an important aspect of LCF studies as it describes the path of the stress amplitude by which the material reaches its final stress level and also gives information about the deformation process during cyclic loading. Cyclic stress response curves at the strain rate of $5x10^{-3}$ s^{-1}, at temperatures of RT, 750^{o}C and 850^{o}C are shown in Figs. 5.2a, 5.2b and 5.3c respectively. Peak tensile stress values are used to demonstrate cyclic stress response. It is noteworthy that at all the temperatures and the strain amplitudes studied, Inconel 617 alloy showed normal cyclic response of increase in cyclic stress amplitude with increase in strain amplitude. At room temperature (Fig. 5.2a), run out was observed at the strain amplitude of ±0.18% and the test was stopped at 1,82,000 cycles. Saturation of peak stress can be observed throughout the test period. At the lower strain amplitudes (<±0.375%), continuous cyclic hardening was observed. There was cyclic softening after hardening during the initial 100–150 cycles at the higher strain amplitudes (≥ ±0.375%) followed by sudden drop in the stress due to initiation and growth of macro cracks leading to final failure. It is important to note that the number of cycles to peak hardening increased with decrease in strain amplitude. It may be seen that at 750^{o}C (Fig. 5.2 b) at the lower strain amplitudes of ±0.20% and ±0.25%, continuous cyclic hardening with

slight change in the rate of hardening is observed followed by saturation. While at the higher strain amplitudes (±0.375% and ±0.50%), there is continuous cyclic hardening with sudden change in the rate of hardening after 500 cycles without any saturation up to the failure i.e. two slope behaviour. It is evident that the number of cycles to peak hardening increased with decrease in strain amplitude. At 850^{o}C (Fig. 5.2c), continuous cyclic hardening is observed at all the strain amplitudes, though no two slope behaviour is observed as in the case of 750^{o}C and very low rate of hardening similar to that observed at RT. It can be concluded that from these curves that Inconel 617 alloy exhibits cyclic hardening behaviour as reported in the previous work in the annealing condition of any alloy [109].

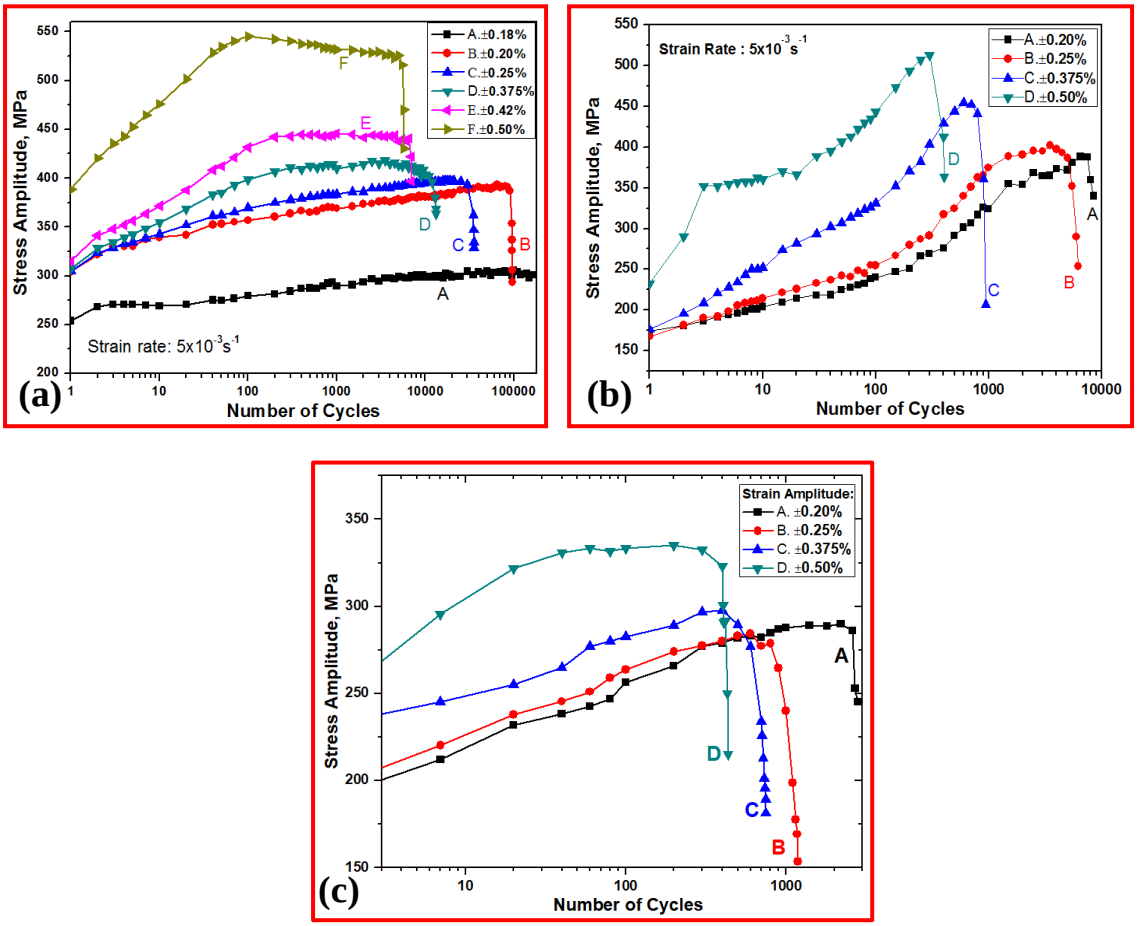

Fig. 5.2: Cyclic stress response curves (peak tensile) of the Inconel 617 fatigue tested samples at: (a) Room temperature (b) 750^{o}C and (c) 850^{o}C.

Figs. 5.3a and 5.3b show the cyclic stress response curves at lower and higher strain amplitudes respectively at three different temperatures which clearly indicate the stress amplitude decreased with increase in temperature. At low strain amplitude 850°C has shown almost same stress amplitude as that at 750°C, whereas at higher strain amplitude the stress amplitude is less than 750°C as normal behaviour. At both the strain amplitudes, the peak stress amplitudes observed are nearly reached the values that are found at RT.

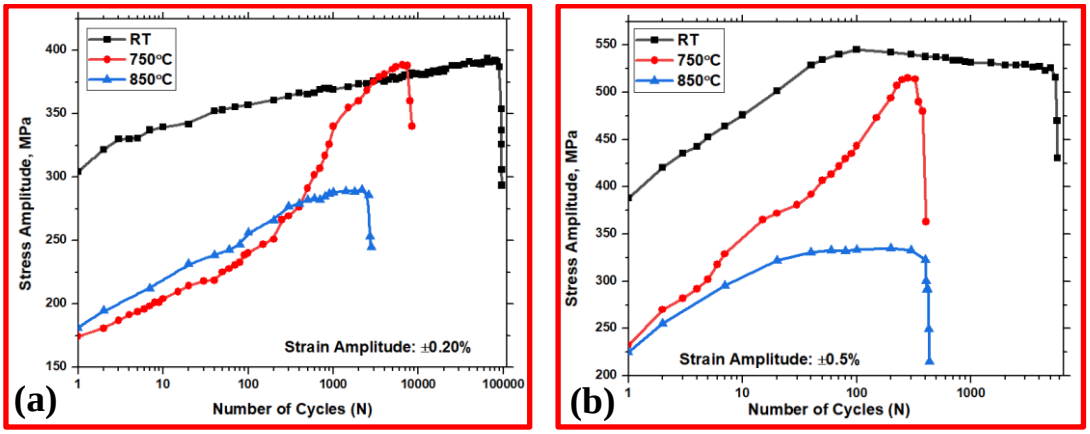

Fig. 5.3: Cyclic stress response curves of fatigue tested samples at RT, 750°C and 850°C at: (a) strain amplitude of ±0.2% (b) strain amplitude of ±0.5%.

During cyclic deformation, the material shows either hardening or softening until the saturation stage is reached. The degree of hardening or softening expressed with respect to first cycle at various test conditions for the half-life cycle was determined using the formula given below [110]:

$$\text{Degree of hardening } (\Delta H) = \frac{(\Delta\sigma/2 \text{ at half-life cycle} - \Delta\sigma/2 \text{ at the first cycle})}{(\Delta\sigma/2 \text{ at the first cycle})} \text{ -------- (5.1)}$$

The values of the degree of hardening value at the half-life cycle are given in Table 5.3 for all the LCF tests conducted. Degree of hardening value was increased at 750°C compared to that at RT but again decreased at 850°C. Fig. 5.4a shows variation of the degree of hardening with strain amplitude. At all the three temperatures, the degree

of hardening increased with increase in strain amplitude, except for the strain amplitude of ±0.5. Fig 5.4b shows the variation of degree of hardening with fatigue life (%) and indicates that at room temperature and 850°C, the degree of hardening was stable after reaching saturation however, at 750°C, with increase in fatigue life there was continuous increase in the degree of hardening. The degree of hardening was more at higher strain amplitude (±0.5%) at room temperature and 850°C whereas interestingly at 750°C, the degree of hardening was high at lower strain amplitude (±0.2%).

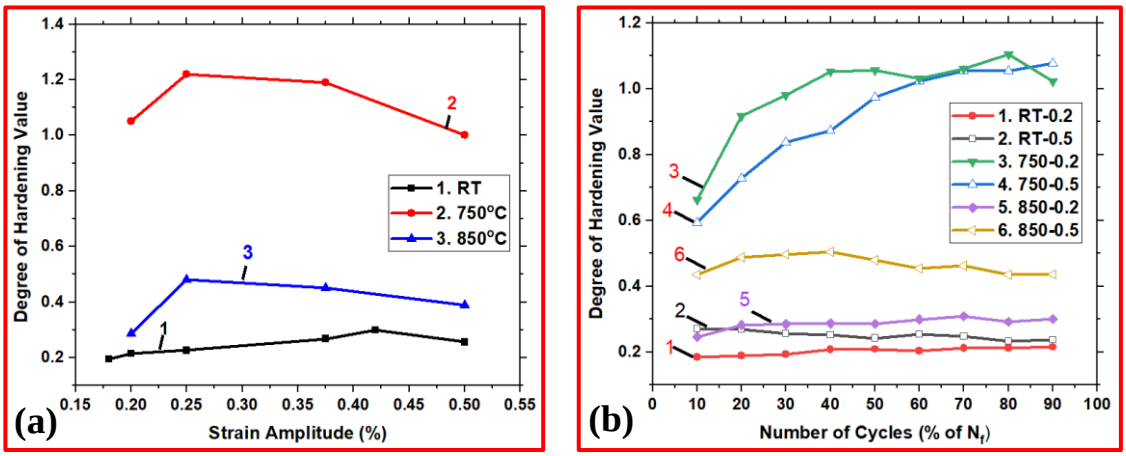

Fig. 5.4: Variation of degree of hardening with respect to: (a) strain amplitude and (b) fatigue life (%) at RT, 750°C and 850°C.

5.5 Cyclic Stress-Strain Behaviour

In LCF, hysteresis loop for each cycle shows relationship between the total strain range and the total stress range. In the present study, the hysteresis loop at half-life is taken as the stable loop [57, 59, 63]. It represents the stable stress-strain behaviour of the material during LCF testing. The width of the hysteresis loop gives plastic strain value. The cyclic stress strain curves can be obtained by connecting the vertices of the stable or half life cycle hysteresis loops at different total strain amplitudes. This method is known as companion method [111]. Multiple step test method [111] can also be used to define cyclic stress-strain curve, where a single

specimen is subjected to constant strain amplitudes until it reaches a stable cycle and then the strain amplitude is increased to a higher level. This process is repeated until sufficient number of stable hysteresis loops are obtained at a given strain amplitude. The tips or vertices of these stable hysteresis loops at different strain amplitudes are connected to form the cyclic stress-strain curve. Strain controlled testing initially started at ±0.15% strain amplitude and continued up to ±1.0% for room temperature and up to ±0.60% for 750^{o}C and 850^{o}C. Fig. 5.5 shows the curves obtained by multiple step test method at three different temperatures.

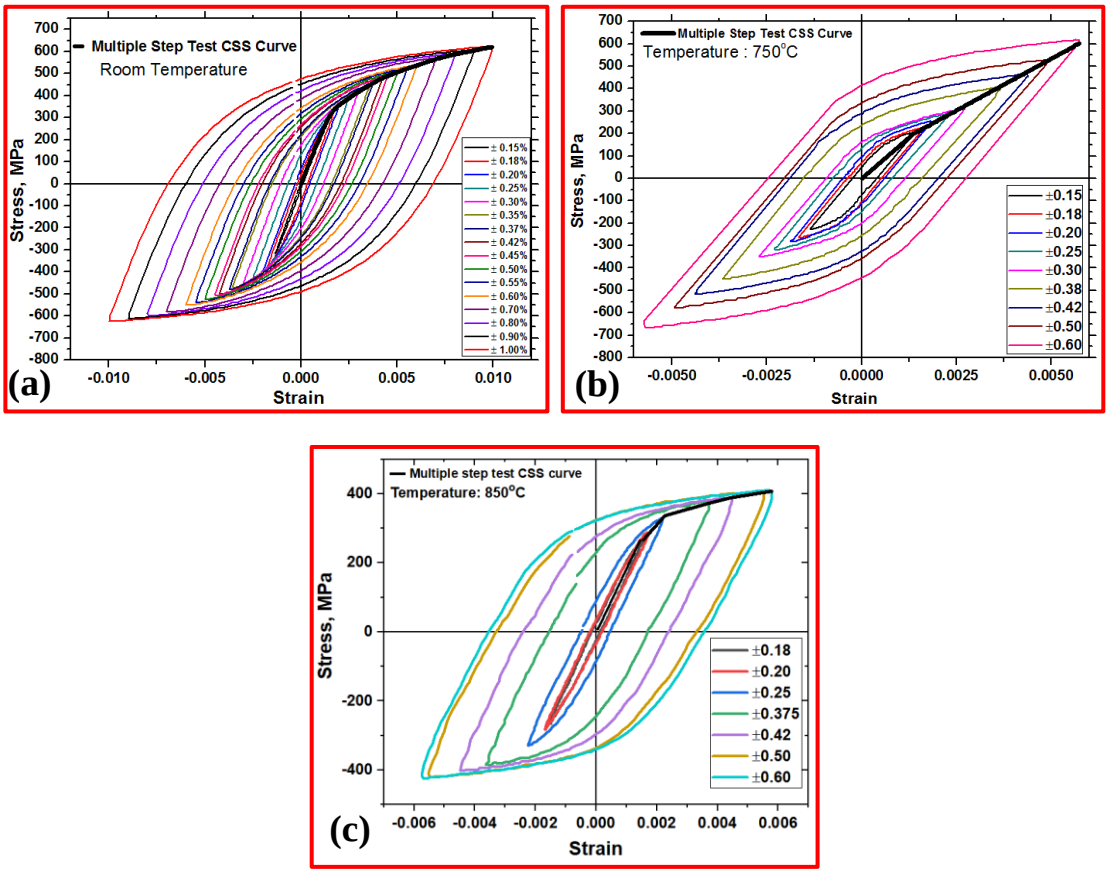

Fig. 5.5: Cyclic stress-strain curves obtained by multiple step test method (MSSS): (a) at room temperature (b) at 750^{o}C and (c) at 850^{o}C.

Fig. 5.6 shows the superimposed monotonic stress-strain curve (MTSS) on cyclic stress strain curves at RT, 750^{o}C and 850^{o}C obtained by companion method (CSS) and multiple step test method (MSSS). It is evident from the plot that the cyclic

curve is above the monotonic curve at all the three temperatures, because of cyclic hardening as can be seen in the stress response curves in Fig. 5.2.

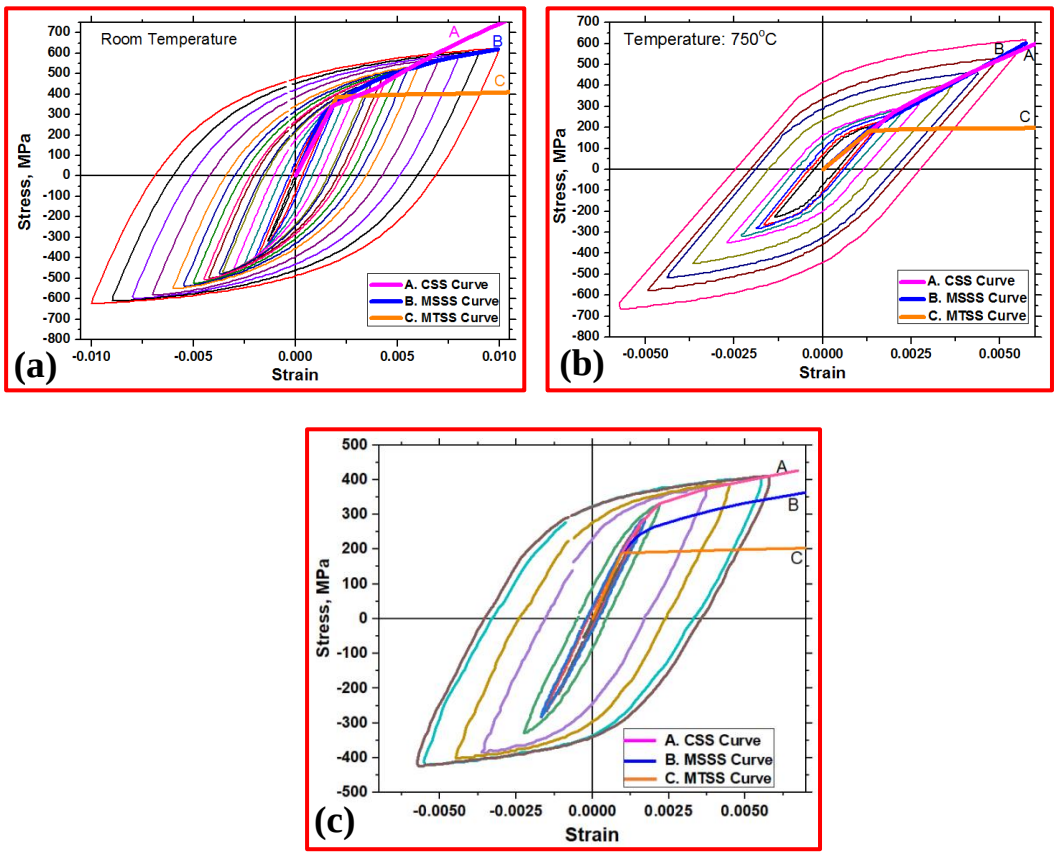

Fig. 5.6: Superimposed monotonic stress-strain (MTSS) curve on Cyclic Stress-Strain curves by companion method (CSS) and by multiple step test method(MSSS), for the samples tested at: (a) RT (b) 750°C and (c) 850°C.

The cyclic stress strain relationship between the stress amplitude ($\Delta\sigma_t/2$) and strain amplitude ($\Delta\varepsilon_t/2$) is given below.

$$\frac{\Delta\varepsilon_t}{2} = \frac{\Delta\varepsilon_e}{2} + \frac{\Delta\varepsilon_p}{2} = \frac{\Delta\sigma_t}{2E} + \left(\frac{\Delta\sigma_t}{2K'}\right)^{1/n'} \quad \text{----------} \quad (5.2)$$

where $\Delta\varepsilon_e/2$ = elastic strain amplitude, $\Delta\varepsilon_p/2$ = plastic strain amplitude, K' = cyclic strength coefficient and n' = cyclic strain hardening exponent. This equation is similar to Ramberg-Osgood equation for monotonic stress-strain relationship. The logarithmic plot of the stress amplitude ($\Delta\sigma/2$) and the plastic strain amplitude ($\Delta\varepsilon_p/2$) is used to obtain these cyclic strength parameters. The best fit linear regression method gives

cyclic strength coefficient (K') and cyclic strain hardening exponent (n') for cyclic loading. The values obtained in the present study at different temperatures are given in Table 5.4. Values of n' and K' increased from RT to those at 750°C and these parameters are quite different from the monotonic tensile test parameters.

Table 5.4: Cyclic Stress-Strain Parameters of Inconel 617 Alloy at RT, 750°C and 850°C.

Temperature	n'	K' MPa
RT	0.13	1039
750°C	0.41	6818
850°C	0.13	706

5.6 Masing and Non-Masing Behaviour

Masing and non-Masing cyclic stress-strain behaviour is an important factor in characterisation of cyclic deformation of a material during low cycle fatigue. Cyclic stress- strain curves demonstrate relationship between the saturated stress and strain amplitudes but they cannot describe the manifestation of hysteresis loop. Masing [112] proposed that the branching in hysteresis loop can be geometrically identical or it can be obtained by magnifying the cyclic stress-strain curve by a factor of two. In order to check whether a material exhibits Masing behaviour or not, the lower tips of the stable hysteresis loops corresponding to different strain amplitudes of the LCF tests are translated to a common origin. For a Masing material, exhibiting Masing behaviour, ascending stages of all these transformed hysteresis loops follow a common envelop or loading path, called Masing curve. Fig. 5.7a shows schematic of typical hysteresis loops that follow common envelop for materials that exhibit Masing behaviour. On the contrary, a material exhibits non-Masing type behaviour when the higher tips of the hysteresis loops do not match with the track of the loading path.

Fig. 5.7b-d shows the envelop curves translated to a common point of origin obtained in the investigated samples at three different temperatures. They reveal mostly non-Masing behaviour, irrespective of the test temperature. At room temperature (Fig. 5.7b), the stable hysteresis loops displayed near Masing behaviour at lower and higher strain amplitude (±0.20% and ±0.5%), and at intermediate strain amplitudes (±0.18%, ±0.25%, ±0.375% and ±0.42%). However, the behaviour was non-Masing type when all the stable loops are together. At 750^{o}C and 850^{o}C (Fig. 5.7c and 5.7d), stable hysteresis loops are not following common envelop at any strain amplitudes i.e. displayed non-Masing behaviour. Over all, non-Masing behaviour can be observed for the alloy Inconel 617 for all the three test temperatures when all the strain amplitudes were considered together.

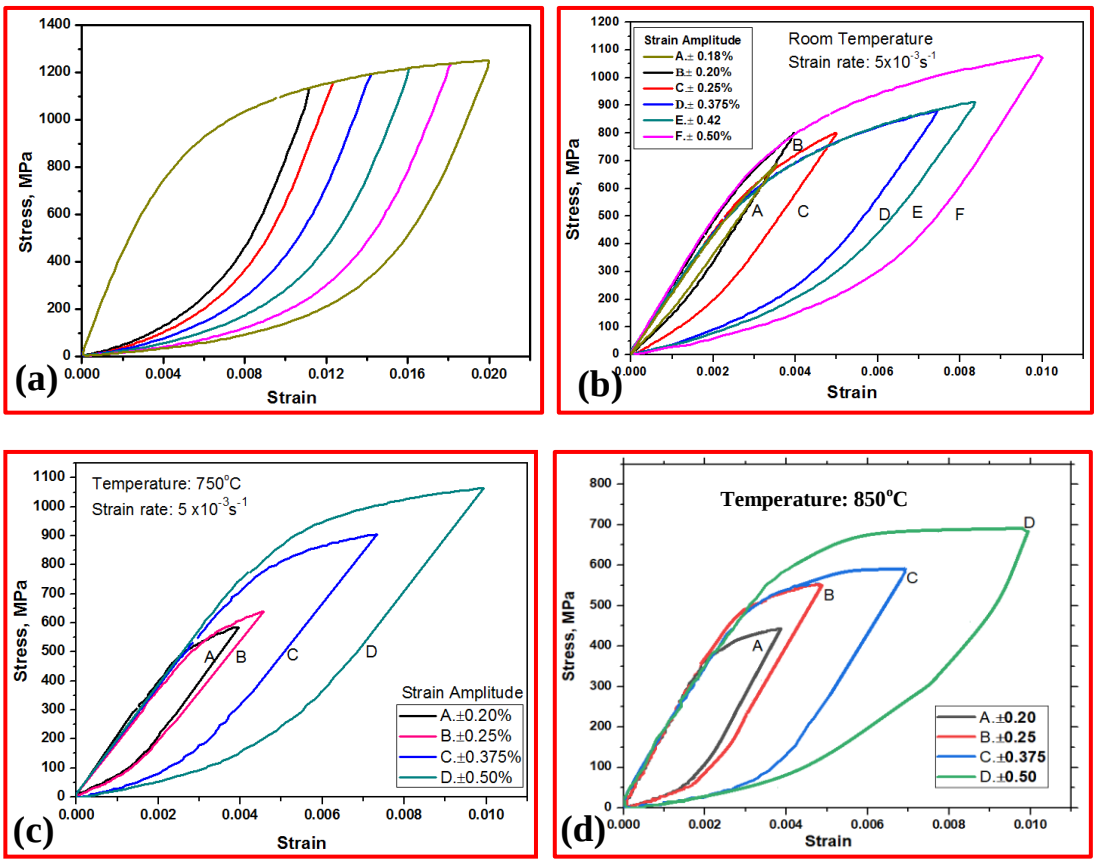

Fig. 5.7: Stress-strain hysteresis loops starting from a common origin and (a) typical hysteresis loops of material exhibiting Masing behaviour. Hysteresis loops obtained in Inconel 617 alloy at: (b) RT (c) 750^{o}C (d) 850^{o}C exhibiting non-Masing behaviour.

5.7 Strain-Life Relationship

The usual way of representing fatigue behaviour of structural materials operating at elevated temperatures and high levels of stress and strain in power generation plant during their in–service period is the strain based LCF life. Variation of the number of reversals to failure ($2N_f$) with elastic strain amplitude ($\Delta\varepsilon_e/2$), plastic strain amplitude ($\Delta\varepsilon_p/2$) and total strain amplitude ($\Delta\varepsilon_t/2$) of Inconel 617 tested at RT, 750°C and 850°C is shown in Fig. 5.8. It is to be noted that the variation of $2N_f$ with $\Delta\varepsilon_p/2$ can be seen as linear straight line on logarithmic scale i.e. it follows Coffin-Manson relationship, given by the equation

$$\Delta\varepsilon_p/2 = \varepsilon'_f (2N_f)^c \qquad \text{----------} \qquad (5.3)$$

where ε'_f and c are fatigue ductility coefficient and fatigue ductility exponent respectively.

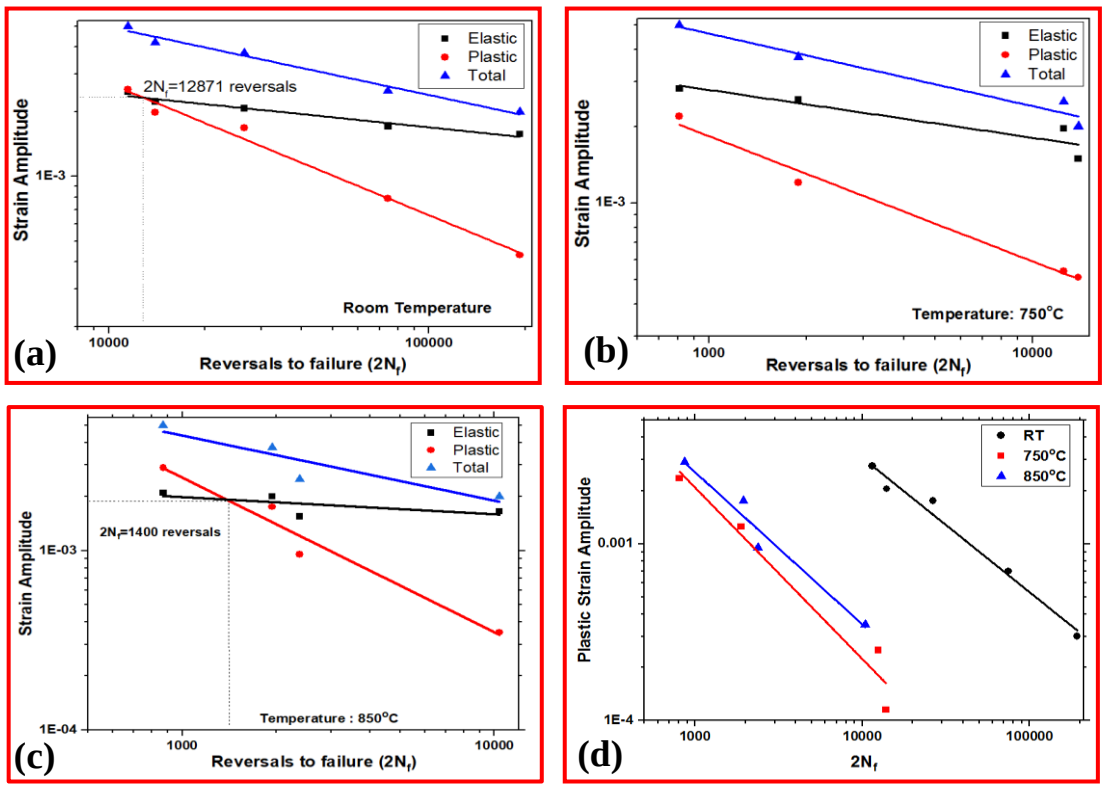

Fig. 5.8: Strain- life curve using Basquin-Coffin-Manson relationship: (a) at RT (b) at 750°C (c) at 850°C and (d) Comparison of Coffin Manson relationship at RT, 750°C and 850°C.

Comparison of plastic strain amplitude-life relationship at both the temperatures is shown in Fig. 5.8d. The fatigue life decreased with increase in temperature. Based on the Basquin and Coffin–Manson relationship, the bi-logarithmic plots of Fig. 5.8a, b and c, plastic and elastic strain amplitudes versus the number of cycles to failure is expressed as shown in the Equation (5.4).

$$\varepsilon_a = \varepsilon_e + \varepsilon_p = \frac{\sigma'_f}{E}\left(2N_f\right)^b + \varepsilon'_f\left(2N_f\right)^c \quad \text{----------} \quad (5.4)$$

where σ'_f is fatigue strength coefficient, 'b' is fatigue strength exponent, ε'_f is fatigue ductility coefficient and 'c' is fatigue ductility exponent [113]. Slope of the plot and intercept on Y-axis at $2N_f = 1$ respectively were determined by least square linear fit of the data in Fig. 5.8a, b and c, to determine the parameter values of low cycle fatigue presented in Table 5.5. All the parameters may be seen to be lower at 850°C with respect to those at RT and 750°C. The *b* and *c* values were calculated also from Morrow's model [114] and Tomkin's model [115] using cyclic strain hardening exponent (n'), and the values are given in Table 5.6 along with values of *b* and *c* of the present investigation. The values derived from both the methods are in agreement, with slight difference.

Table 5.5: Parameters for Strain Life Relationship and Plastic Strain Life Relationship for Inconel 617 Alloy Fatigue Tested at RT, 750°C and 850°C.

Temperature	σ'_f MPa	*b*	ε'_f	*c*
RT	2300	-0.154	0.5031	-0.761
750°C	1632	-0.188	0.2318	-0.970
850°C	872	-0.149	1.0664	-1.204

Table 5.6: Values of Fatigue Strength (*b*) and Ductility (*c*) Exponents, and Calculated Values from Morrow's and Tomkins's model for Inconel 617 Alloy.

Temperature	*b* Observed	*b* Morrow	*b* Tomkins	*c* Observed	*c* Morrow	*c* Tomkins
RT	-0.154	-0.095	-0.103	-0.761	-0.603	-0.793
750^{o}C	-0.188	-0.142	-0.225	-0.970	-0.851	-0.649
850^{o}C	-0.149	-0.130	-0.128	-1.204	-0.827	-0.725

5.8 Strain Energy–Life Relationship

Since the low cycle fatigue damage is generally associated with cyclic plastic strain, the plastic strain energy plays an important role in prediction of fatigue life of components. Hence, the idea of relating fatigue life to the energy dissipated per unit volume or the plastic work done during the cyclic loading has been proven more effective in describing the LCF behaviour [116]. In general, the area of hysteresis loop at half-life cycle is considered as the average plastic strain energy per cycle (ΔW_p), Total plastic strain energy (ΔW_t) is the summation of the plastic strain energy (ΔW_p) and the tensile elastic strain energy (ΔW_e). Figs 5.9a-c shows plots of the plastic strain energy and total strain energy with reversals to failure ($2N_f$) at the three temperatures. It is understood from the plots that at room temperature the plastic strain energy is lower compared to those at higher temperatures. The parameters derived from the linear regression analysis for relationship of plastic and total strain energies with reversals to failure are given in the Table 5.7, where W'_f and β are material constants and β is related to the fatigue life constant ($\beta = b + c$) [117].

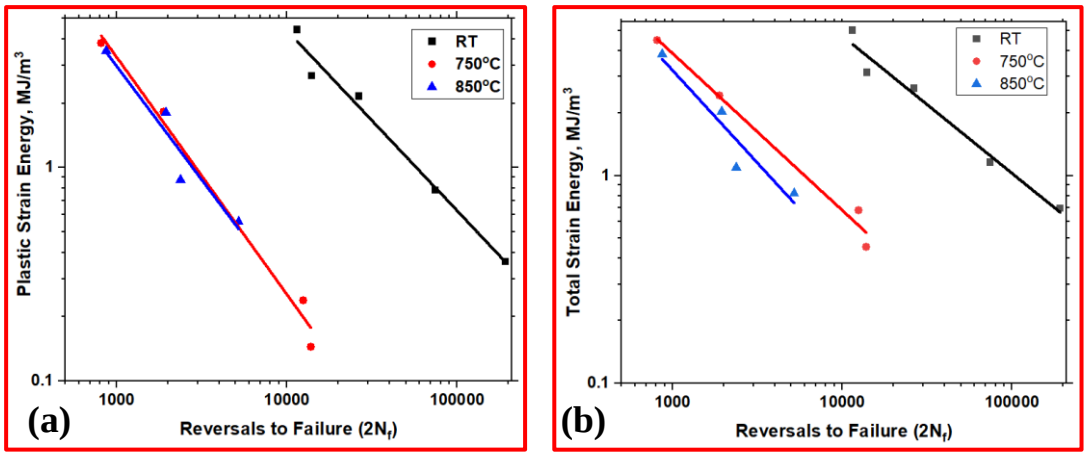

Fig. 5.9: Strain energy - life relationship using experimental values at RT, 750°C and 850°C: (a) plastic strain energy (W_p) and (b) total strain energy (W_t).

Table 5.7: Parameters for Strain Energy-Life Relationship for Inconel 617 Alloy Fatigue Tested at the Three Temperatures.

Temperature	Plastic strain energy		Total strain energy	
	W'_f	β	W'_f	β
RT	10568	-0.845	2087	-0.661
750°C	7164	-1.112	720	-0.756
850°C	4666	-1.064	1510	-0.891

Plastic strain energy per cycle (ΔW_p) can be calculated as described in the references [117-122]. For the material exhibiting Masing behaviour, the hysteresis plastic energy per cycle ΔW_p is the area of the hysteresis loop and it can be calculated directly using cyclic stress strain curve Equation (5.2) established earlier [122].

$$\Delta W_p = \left(\frac{1-n'}{1+n'}\right) \Delta\sigma\Delta\varepsilon_p \qquad \text{----------} \quad (5.5)$$

where, n' is the cyclic strain hardening exponent, $\Delta\sigma$ is the total stress range, and $\Delta\varepsilon_p$ is the plastic strain range. For non-Masing materials, matching the upper branches of the hysteresis loops by translating the original position of each loop along its linear response portion gives one master curve as shown in Figs. 5.10a, c and e. By using this

master curve, Jhansale and Topper [123] developed an equation for calculating the plastic strain energy of non-Masing material as given below.

$$\Delta W_p = \left(\frac{1-n^*}{1+n^*}\right) \Delta\sigma\Delta\varepsilon_p + \left(\frac{2n^*}{1+n^*}\right) (\delta\sigma_o \, \Delta\varepsilon_p) \quad \text{----------} \quad (5.6)$$

where n^* is the hardening exponent of the master curve and $\delta\Delta\sigma_o = \Delta\sigma - \Delta\sigma^*$, is increase in the proportional stress range due to non-Masing behaviour of the material. The value of n^* is quite different from the cyclic strain hardening exponent n' in Equation (5.2). The values of n^* at room temperature, 750°C and 850°C are 0.58, 0.65 and 0.60 respectively. The plots of plastic strain energy calculated using Equation (5.5) and (5.6) with reversals to failure for the samples tested at RT, 750°C and 850°C are shown in Figs. 5.10b, d and f respectively along with the parameters obtained.

It is evident from the plots that plastic strain energy values calculated using equations are close to the experimental values at room temperature but varied much at 750°C and 850°C, though the values are in range. The values calculated using Equation (5.6) were found to be closer to the experimental values compared to those estimated using the Equation (5.5) at the three temperatures due to non-Masing behaviour of this material.

5.9 Role of Friction and Back Stress

To describe dislocation interactions or movement during strain controlled fatigue studies, friction stress and back stress are important parameters. These two internal stresses can provide information related to the origins of the cyclic softening or hardening behaviour of polycrystalline metals during low cycle fatigue conditions. Friction stress (σ_f) describes the expansion or contraction of the elastic domain, which is

related to the isotropic hardening of materials and arises from the resistance to dislocation movement in the lattice which involves short range interaction obstacles.

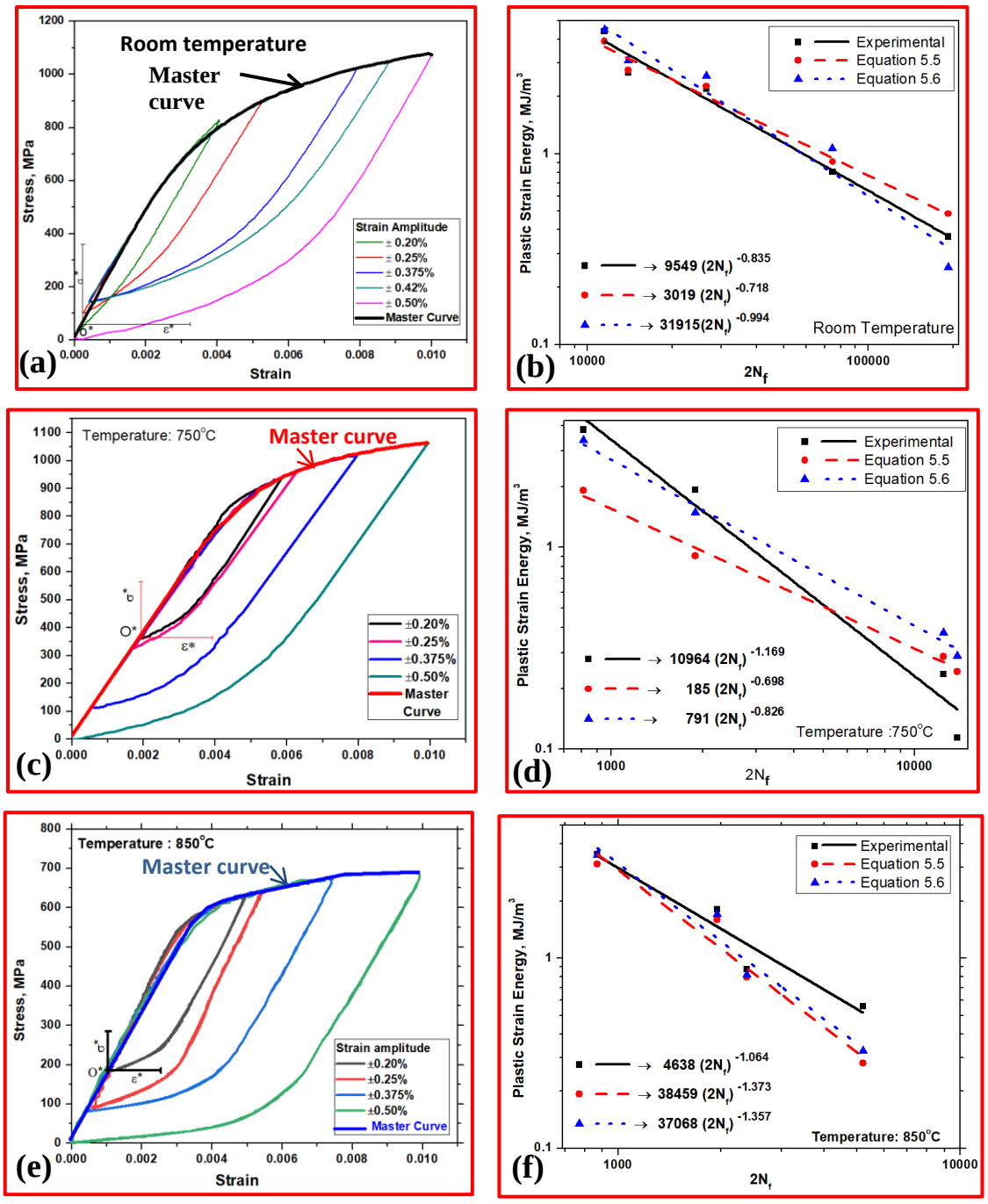

Fig. 5.10: Construction of master curves from stable hysteresis loops at (a) Room temperature (c) 750°C and (e) 850°C. Comparison of strain energy life experimental data with the values calculated from Equation (5.5) and Equation (5.6) for the samples tested at (b) Room temperature (d) 750°C and (f) 850°C.

Whereas back stress (σ_b) represents the translation of the yield surface in the stress space in macrostructure, corresponds to the kinematic hardening of materials. And it is linked to the local straining process that introduces long range interaction with mobile dislocations [124]. The precipitates, foreign atoms, lattice friction and other dislocations act as short-range obstacles.The long range impenetrable obstacles can be the sub grain boundaries. As per the Cottrell's definition [125], the back stress (σ_b) and the friction stress (σ_f) parameters can be calculated directly from the stress- strain hysteresis loop. σ_f is determined at a reversed plastic strain offset of 0.01% as shown in Fig. 5.11, as per the procedures described elsewhere [117, 124, 126]. The back stress, σ_b, can be then obtained by using the equation, $\sigma_b = \sigma_a - \sigma_f$, where σ_a is stress amplitude. In the present study, friction stress and back stress were determined for low (±0.2%) and high (±0.5%) strain amplitudes at both temperatures, at several representative fatigue cycles, to find out their contribution to cyclic stress response of the Inconel 617 alloy.

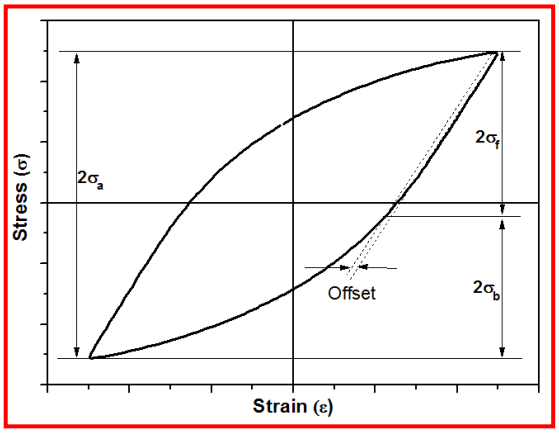

Fig. 5.11: Determination of friction stress and back stress from fatigue hysteresis loop.

Figs. 5.12a and b shows the variation of friction stress and back stress with number of cycles at RT and 750^{o}C respectively. With increasing temperature, both the friction stress and back stress are decreased. Both stresses decreased with decrease in

strain amplitude. It is convincing from the plot that, for high strain amplitude at room temperature initial hardening and further softening is observed as per the stress response curves (Fig. 5.3a). For low strain amplitude, stable hardening behaviour is observed. At 750^{o}C, for both the strain amplitudes, increase in both the stresses with number of cycles, indicating hardening behaviour as observed in the stress response curves (Fig. 5.3b). Due to precipitation of carbide particles after few initial cycles, the interaction between dislocations and these carbides, increasing both the friction and back stress. Similar behaviour is observed at 850^{o}C as that of RT.

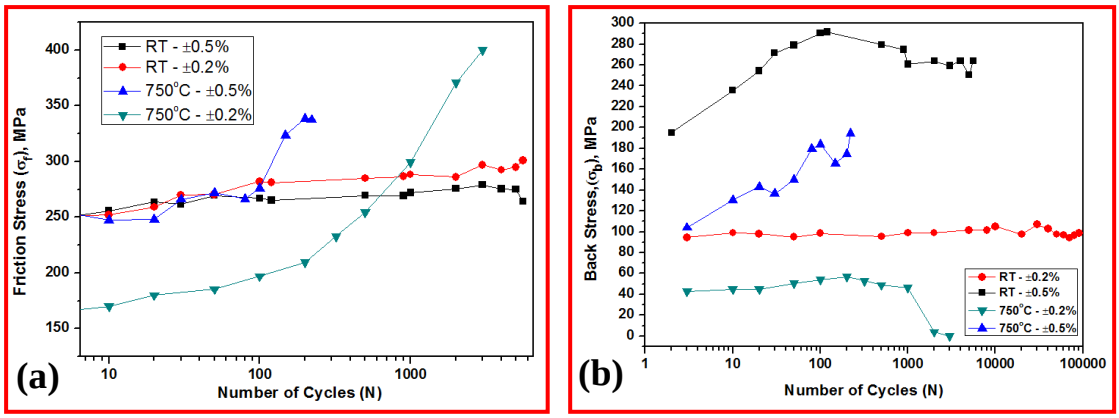

Fig. 5.12: (a) Friction stress with respect to number of cycles (N) for low and high amplitudes at RT and 750^{o}C and (b) back stress with respect to number of cycles (N) for low and high amplitudes at RT and 750^{o}C.

5.10 Deformation Behaviour

Information related to microstructural changes during cyclic deformation at different temperatures is currently very limited for the Inconel 617 alloy. As the strain amplitude changes, the cyclic deformation behaviour i.e. cyclic hardening or softening varies due to change in the dislocation substructure. TEM analysis was done on the fractured samples tested in LCF at higher and lower strain amplitudes. Dislocation substructure of the samples tested in fatigue at room temperature at the lowest (±0.20%) and highest (±0.50%) strain amplitudes are shown in Fig. 5.13 and Fig. 5.16

respectively. The most frequently observed deformation structure consists of planar array of dislocations and dislocation pairs. The substructure is highly heterogeneous with packets of dislocation debris and ill-defined cells at low strain amplitude (±0.2%) as shown in Fig 5.13a. The cell size is very small at lower strain amplitude compared to that at the higher strain amplitude. The microstructure also contains micro twins of width of 0.1 μm - 0.2 μm. These micro twins contain well defined dislocation lines oriented in same direction (Fig 5.13b). Similar observations were made by Burke et al [61] in the same alloy under low cycle fatigue conditions. Multiple annealing twins were observed at this strain amplitude. Carbide bands were also observed which are parallel to each other and compressed to thin structures as needles as shown in Fig. 5.13b. The dark field TEM micrograph shown in Fig 5.13c is an indication of interaction of dislocations with stacking faults. These interactions are responsible for the formation of micro twins as seen in Fig. 5.13b. This has been reported earlier for Nickel and Cobalt based alloy at the same strain amplitude as in the present case [127]. Such interaction can create hindrance to movement of dislocations which in turn causes strain hardening.

Needle-like carbide precipitates (Fig. 5.13d) with widths of the order of 20 nm were observed, that were primarily converted from the round or cuboid shaped carbide particles, initially present along the grain boundaries. During cyclic loading, they get aligned parallel to each other. The diffraction pattern shown in Fig. 5.13e confirms the carbide particles of $M_{23}C_6$. Similar carbide precipitates have been reported by Rao et al. [57] for the same alloy, fatigue tested at 850^{o}C.

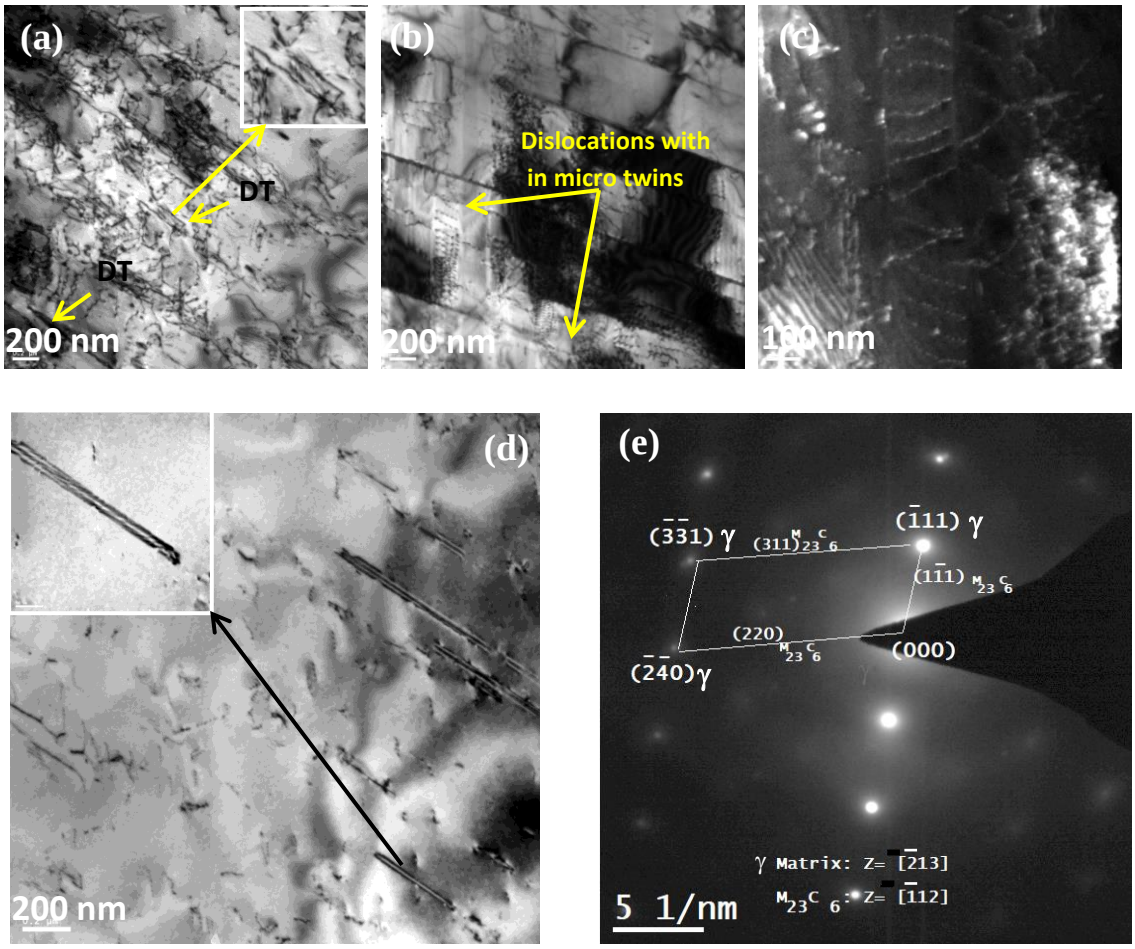

Fig. 5.13: TEM micrographs of the fatigue sample tested at room temperature and at ±0.20% strain amplitude showing: (a) Dislocation network with ill-defined cell structure and arrow (DT) indicates deformation twins, (b) micro twins with array of aligned dislocations within and carbide particle bands, (c) Interaction of stacking fault with dislocations beside micro twins (dark field image) (d) aligned needle shape carbide particles in the matrix and (e) SAED pattern from the micrograph shown in (d).

Two interrupted LCF tests were conducted at room temperature for ±0.5% strain amplitude, one up to 80 cycles (during hardening) and the other up to 1500 cycles (during softening) to find out the deformation mechanism of this alloy during initial hardening and subsequent softening. TEM micrographs of the samples tested up to 80 and 1500 cycles are presented in Figs. 5.14 and 5.15 respectively. Fig. 5.14a shows formation and alignment of dislocations in slip bands of 0.55 μm-0.65 μm width. The dislocations created at this stage were primarily confined to one glide plane (111) and

accumulated in the slip band oriented in {110} direction. The slip bands are uniformly distributed. Cross slip bands of the same slip system also began to form at this stage of deformation as shown by arrow. Fig. 5.14b shows magnified view of these bands clearly revealing formation of pairs of dislocations within the substructure (see arrow). Fig. 5.14c shows magnified view of the low dislocation density. There is no indication of fresh precipitation or interaction of precipitates and dislocations. Fig. 5.15a shows TEM micrographs corresponding to the softening stage (1500 cycles) where there is an increase in number of slip bands as well as dislocation density. The slip band width has also decreased and is found to be 0.08 μm to 0.1 μm. Formation of cross slip bands of the same slip system is observed to be prevalent at this stage of softening compared to that of the hardening stage. The angle between slip bands is 70.5^{o}, an expected value for the <111> family. Fig. 5.15b shows a high density of dislocations in the slip bands. Fig 5.15c shows elongated cells apart from multiple sets of extended pairs of dislocations (see arrow).

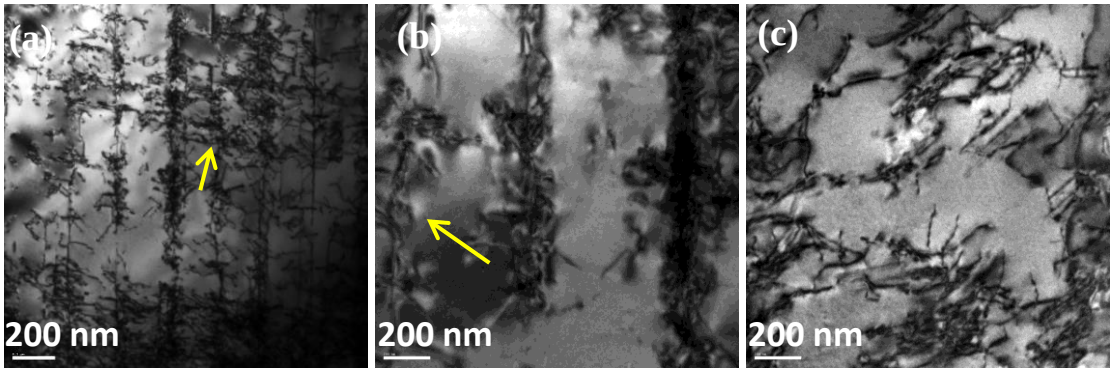

Fig. 5.14: TEM micrographs of the fatigue sample tested at room temperature and at ±0.50% strain amplitude, test interrupted at 80 cycles (hardening) showing: (a) formation of slip bands with uniform distance and arrow indicates cross slip band formation, (b) magnified view of dislocations within slip band indicating pairs of dislocation and (c) low density of dislocations compared to that of the softening region.

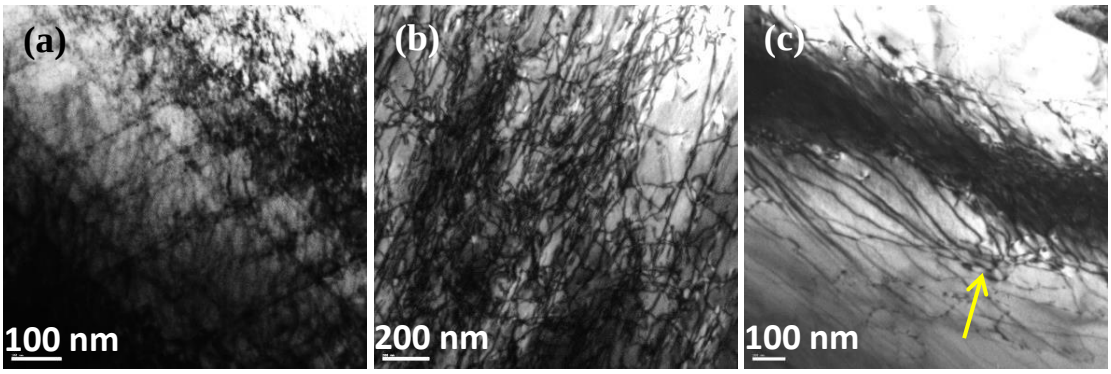

Fig. 5.15: TEM micrographs of fatigue sample tested at room temperature and at ±0.50% strain amplitude, interrupted at 1500 cycles (softening) showing: (a) increase in number of slip bands with high density with in and cross slip band formation, (b) very high density of dislocations formed at some places of the sample and (c) extended pairs of dislocations shown by arrow.

TEM micrographs of the samples tested up to fracture clearly indicate arrays of dislocations and dislocation- dislocation interaction in Fig. 5.16. Well-defined cells were observed in the sample tested at higher strain amplitude till fracture (Fig.5.16b). The regions between the dislocation cells are almost entirely devoid of free dislocations. The cell size is much larger than that of cells in the samples tested at lower strain amplitude. A magnified view of the alignment of dislocations along [110] direction as well as pairs of dislocations are depicted in Fig. 5.16c. Intersections of dislocations are also found at both the strain amplitudes. No precipitate-dislocation interactions are found at this temperature, at both the strain amplitudes.

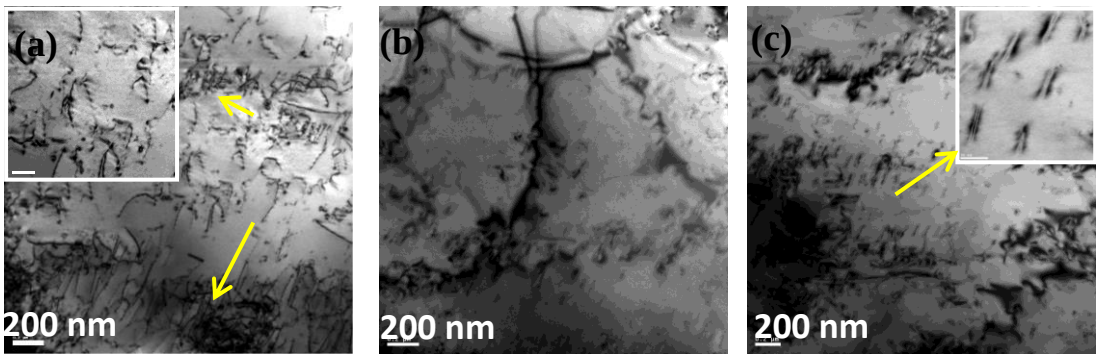

Fig. 5.16: TEM micrographs of the fatigue sample tested at room temperature and at ±0.50% strain amplitude showing: (a) intersection of dislocations and alignment of dislocations (arrows), (b) increased cell size compared to that at ±0.20% strain amplitude and (c) pairs of dislocations.

TEM micrographs of the samples tested at 750^{o}C at low strain amplitude are shown in Fig. 5.17. With increase in the test temperature to 750^{o}C, the density of dislocations is increased (Fig. 5.17a) but the dislocations are distributed more uniformly unlike those at low temperature where segregation of dislocation pileups were noticed. Well-defined network of dislocation sub structure is observed. High dislocation density, dislocation-dislocation interaction and bowing of dislocations are clearly seen at this stage (Fig 5.17b). Distinct network of dislocations is also observed due to the intersections of dislocations with fine precipitate particles formed at this temperature during cyclic deformation. This micrograph also shows a single carbide particle interaction with dislocations (shown by white arrows). Dislocation pileups are generally the preferred sites for the precipitation [57]. Fig. 5.17c shows very fine precipitates of $M_{23}C_6$ carbides, re-precipitated throughout the structure. γ' particles can be also be observed at this temperature along with carbide particles of different shapes. Fig 5.17d shows diffraction pattern from which the well-known cube-on-cube orientation relation between the fcc γ matrix and $M_{23}C_6$ precipitates could be established. These interactions between precipitate particles (carbide and γ' particles) and dislocations are the prime reason for increase in the rate of hardening.

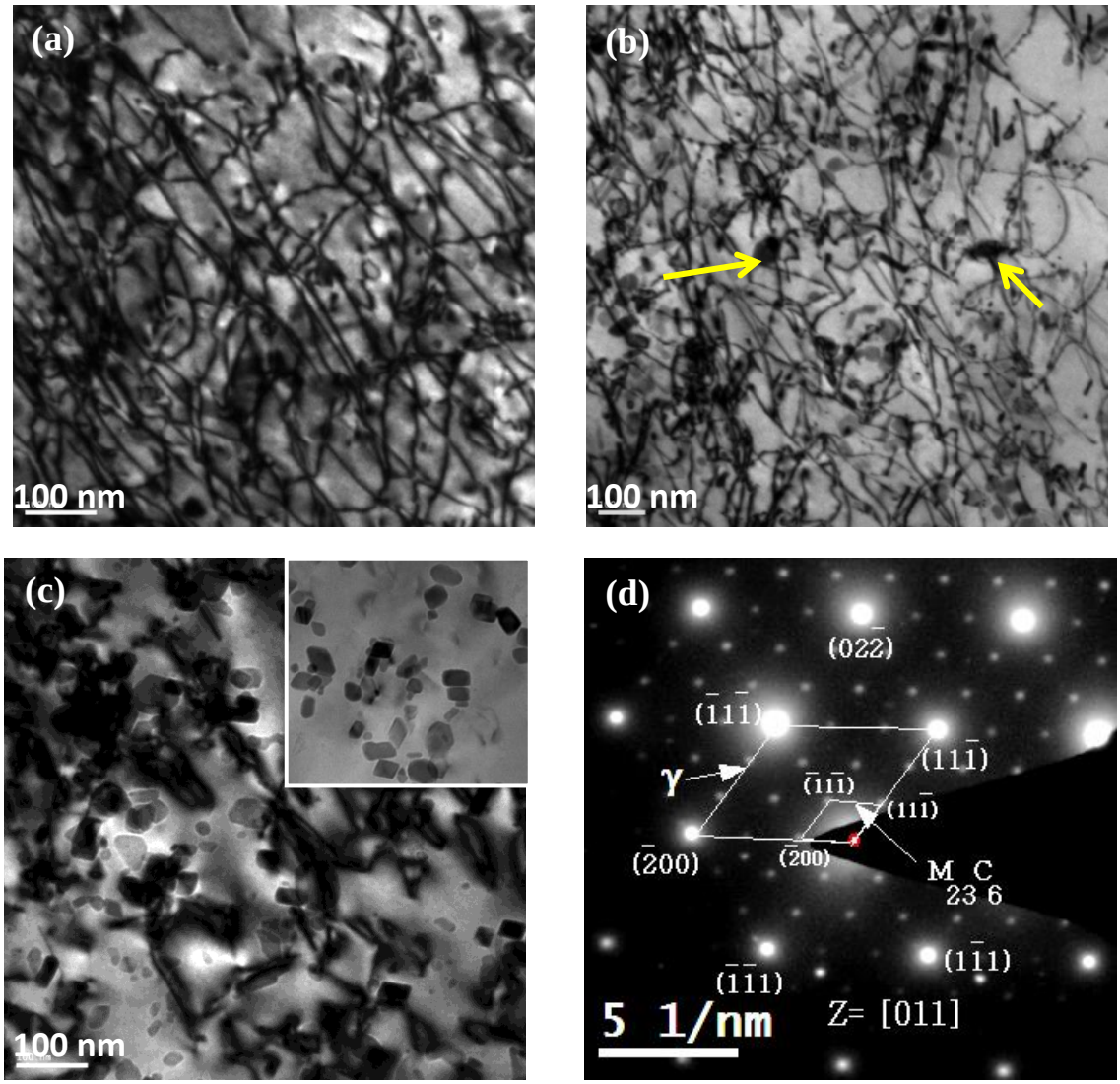

Fig. 5.17: TEM micrographs of the fatigue sample tested at 750^{o}C and at ±0.20% strain amplitude showing: (a) Increase in dislocation density and elongated sub grain formation with thick walls, (b) well defined interaction of precipitates with dislocations, as shown by arrow, (c) fine precipitates uniformly distributed in the matrix (d) SAED pattern of the carbide particles within matrix clearly showing cube on cube orientation relation.

Fig 5.18 shows TEM micrographs of the samples tested at 750^{o}C at high strain amplitude (±0.5), indicating decrease in the density of dislocations and cell size (Fig. 5.18a). The volume fraction of precipitates observed is less and also they are widely spaced due high strain amplitude and short duration of the test. Fig 5.18b shows a magnified view of the cells. Fig. 5.18c shows carbide and γ′ particles in the matrix of γ. These particles were observed at both the strain amplitudes only the size is bigger and

volume fraction is less at this strain amplitude. Fig. 5.18d shows diffraction pattern of γ′ particle (Ni_3(Ti,Al)) observed.

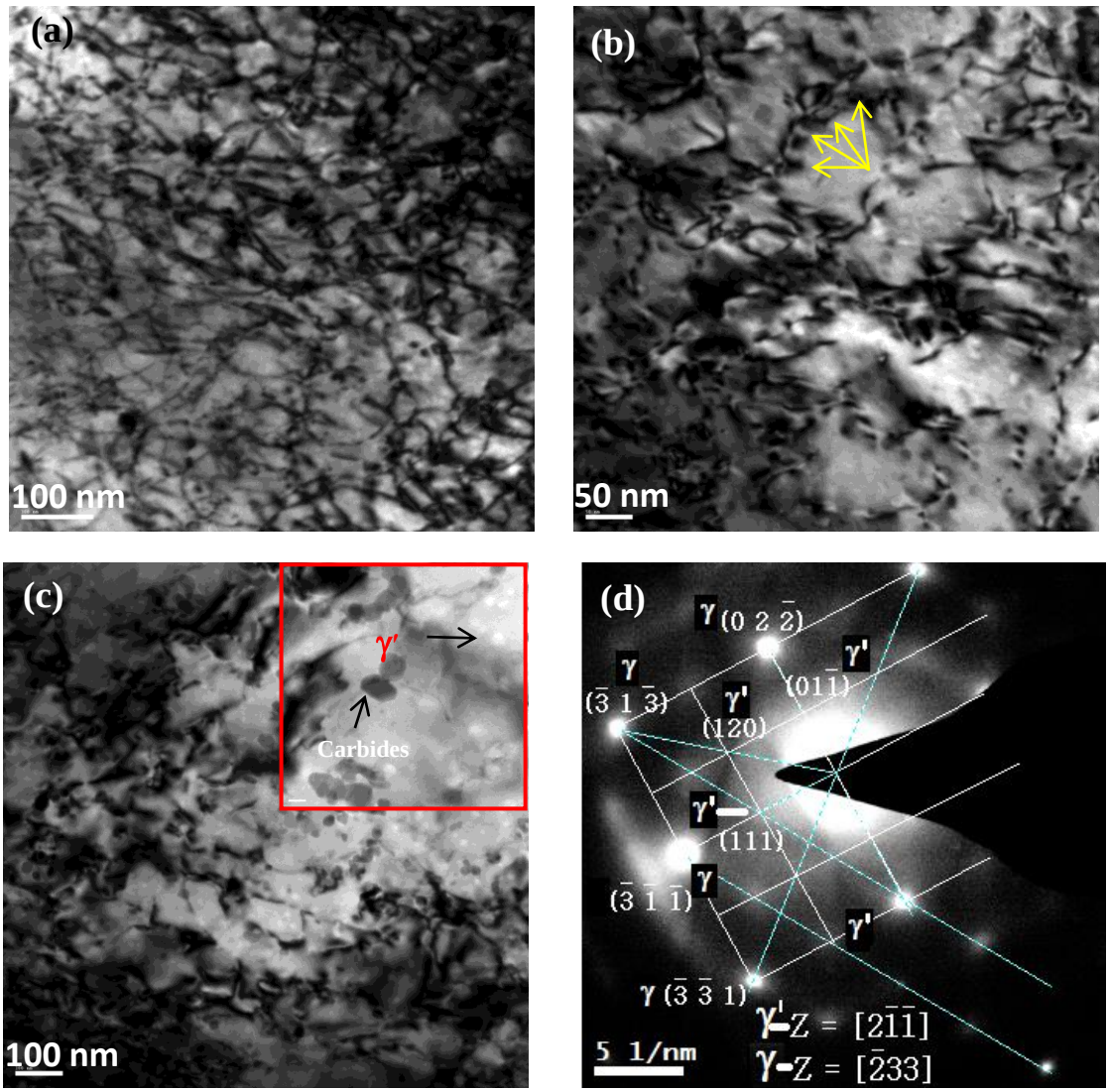

Fig. 5.18: TEM micrographs of the fatigue sample tested at 750°C and at ±0.50% strain amplitude showing: (a) decrease in dislocation density and smaller elongated cell structure with thin walls, (b) magnified view of the cells, (c) Precipitates unevenly distributed in the matrix and (d) SAED pattern of Ni_3(Ti,Al) particle observed.

Figs. 5.19 and 5.20 shows TEM micrographs of the samples fatigue tested at 850°C and at strain amplitude of ±0.2% and ±0.5% respectively, clearly indicate precipitation of carbides which are bigger in size and randomly distributed in the microstructure. These precipitates contributed for increase in stress amplitude for the subsequent cycles. Number of precipitates decreased with increase in strain amplitude.

The rate of work hardening is low compared to that at 750°C due to the reduction in number of precipitates, and degree of hardening compared at the half life cycle is also low. At low strain amplitude, micro twins can be observed (Fig. 5.19a) - shown by arrow) in which aligned dislocations can also be seen. Dislocation density decreased compared to that at RT and 750°C.

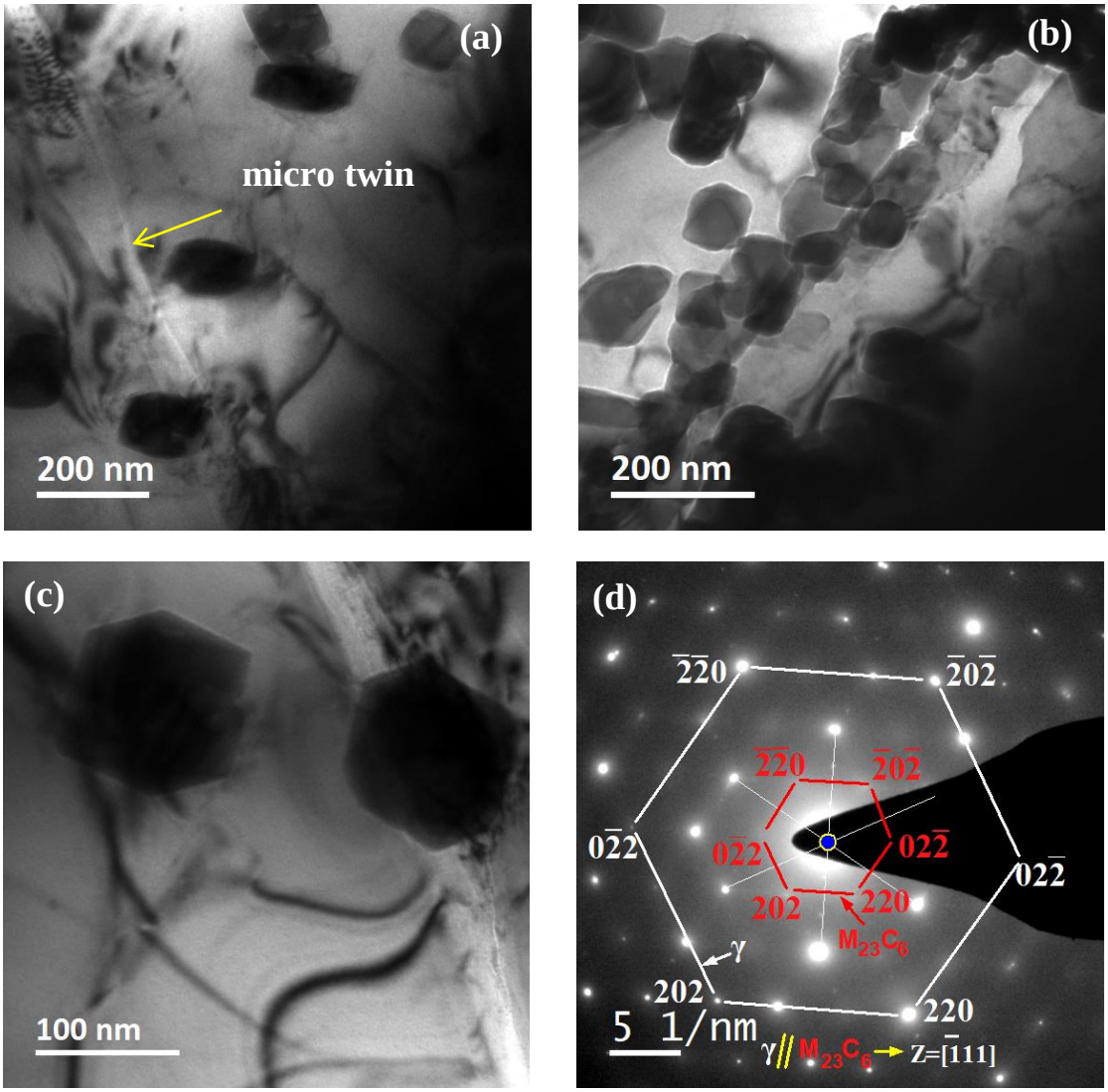

Fig. 5.19: TEM micrographs of the fatigue sample tested at 850°C and at ±0.20% strain amplitude showing: (a) precipitates formed which are bigger in size compared to that formed at 750°C (b) precipitate interaction with dislocations (c) magnified view of the carbide particles and (d) SAED pattern confirming the carbide particles to $M_{23}C_6$ carbides. Presence of γ′ is not observed at this temperature.

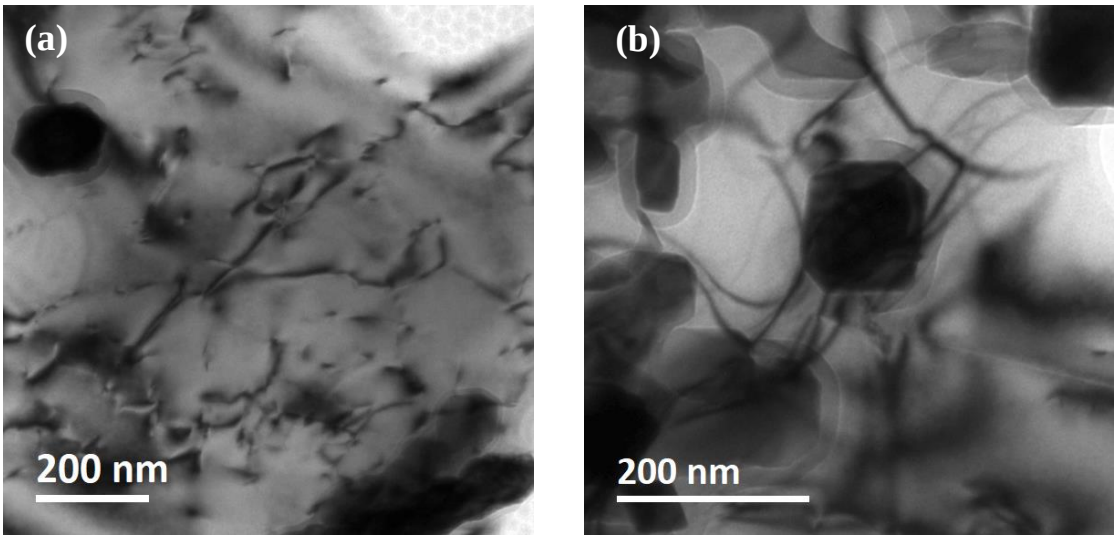

Fig. 5.20: TEM micrographs of the fatigue sample tested at 850^{o}C and at ±0.50% strain amplitude showing: (a) precipitates formed which are bigger in size compared to that formed at 750^{o}C (b) magnified view of the carbide particle.

5.11 Surface Morphology

Fig. 5.21a shows surface morphology of the cylindrical surface of the fatigue specimen tested at room temperature, close to fracture end. The slip bands terminating on the surface can be seen at a higher magnification in Fig 5.21b. It is important to note that very fine micro cracks of small length were visible on the surface. Fig 5.22 shows surface morphology of the samples tested at 750^{o}C with larger crack length and width. The surface does not contain any oxidized particles. Similar observations were noticed at 850^{o}C.

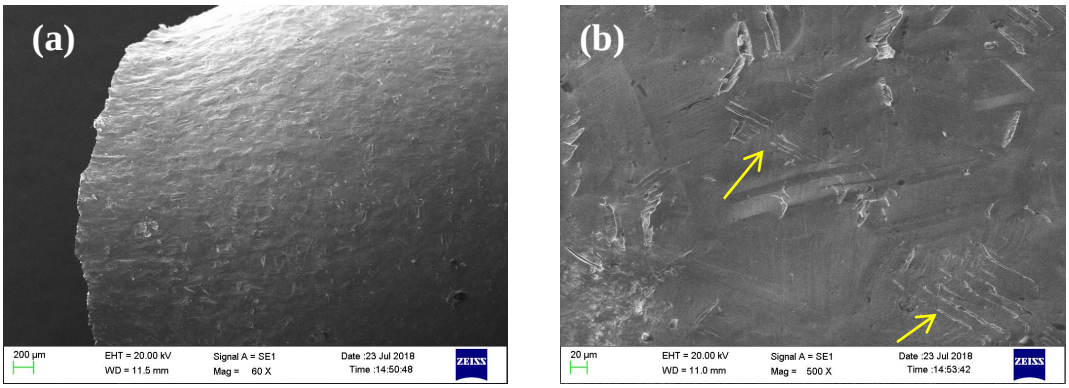

Fig. 5.21: SEM micrographs showing surface morphology of the samples fatigue tested at room temperature, and at strain amplitude of ±0.5%. Arrows indicate slip bands formed on the surface.

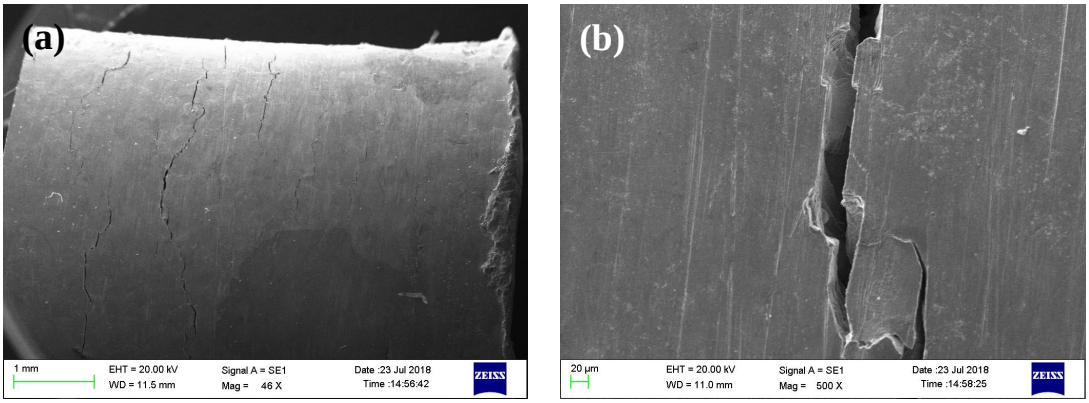

Fig. 5.22: SEM micrographs showing surface morphology of the samples fatigue tested at 750^{o}C and at strain amplitude of ±0.5%.

5.12 Fracture Behaviour

After fatigue testing, fracture surfaces of all the samples tested at RT, 750^{o}C and 850^{o}C at different strain amplitudes were examined and analysed using scanning electron microscopy (SEM). Figs 5.23 and 5.24 show fatigue crack initiation sites (shown by arrows) in the samples tested at room temperature at low (±0.2%) and high (±0.5%) strain amplitudes respectively. At this temperature, stage I crack initiation is featureless. A significant difference in fracture behaviour of the alloy at low and high strain amplitudes is observed during the stage II i.e. crack growth stage. The striations are well defined and uniformly spaced at high strain amplitude compared to those at low strain amplitude. Secondary micro cracks were observed at the junctions of ridges or

ratchet lines for high strain amplitude. At low strain amplitude, the striations are not uniform throughout the tear ridges and appear partially deformed or ductile (see arrow). It clearly indicates that the crack propagation might have been easily arrested and repetitively resumed only after a certain number of cycles. The stage II crack propagation is highly facilitated by increase in strain amplitude from ±0.2% to ±0.5%. The average inter-striation spacing in stage II was found to increase with increase in strain amplitude. The spacing is 2-3 μm at ±0.2% strain amplitude and 4-5 μm at ±0.5% strain amplitude. The area of the fatigue crack growth zone is nearly 50% of the area at ±0.2% and 40% at ±0.5%.

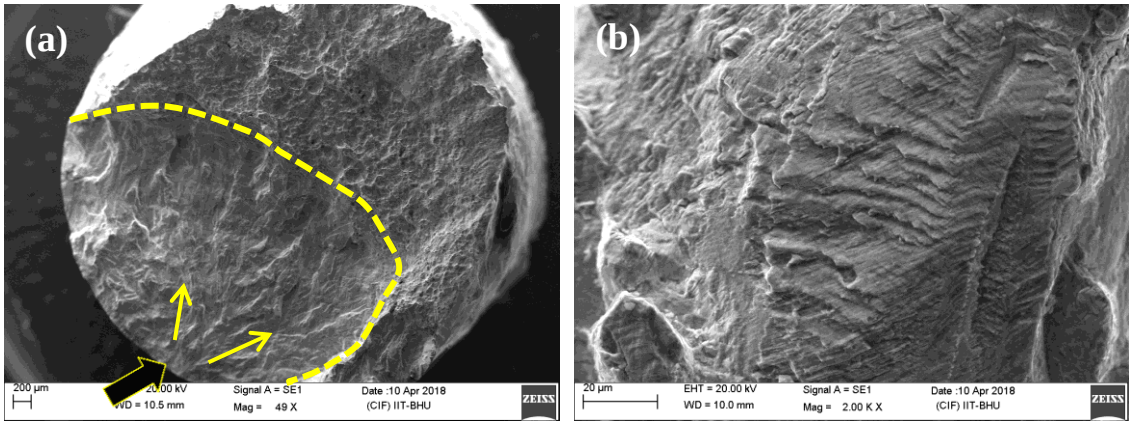

Fig. 5.23: SEM fractographs of the samples fatigue tested at room temperature and at strain amplitude of ±0.20% showing: (a) crack initiation site (dark arrow) and growth direction (light arrow) and (b) striation morphology

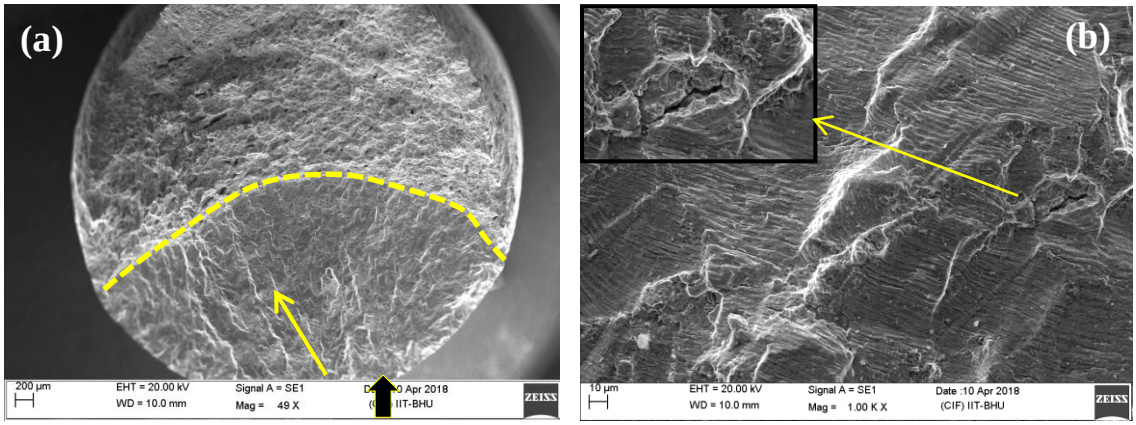

Fig. 5.24: SEM fractographs of the samples fatigue tested at room temperature and at strain amplitude of ±0.50% showing: (a) crack initiation site (dark arrow) and growth direction (light arrow) and (b) striation morphology and minor secondary crack.

Figs 5.25 and 5.26 show fracture surfaces of the samples tested at 750^{o}C at strain amplitudes of ±0.2% and ±0.5% respectively. Crack initiation sites are shown by thick arrows. The crack initiation region is flat for some distance inside and can be clearly seen. In the case of high strain amplitude, the stress concentration at some of the boundaries, arising from the higher applied strains led to intergranular cracking in some regions but most of the crack propagation is transgranular. Though secondary micro cracks are more as compared to that at room temperature, these cracks are more in number compared to those at lower strain amplitude. Cleavage facets were also seen at higher strain amplitude with intergranular cracks. The rapid drop in stress amplitude observed prior to failure is mainly attributed to fast growth and eventual coalescence of such cracks resulting in reduction in the load bearing capacity.

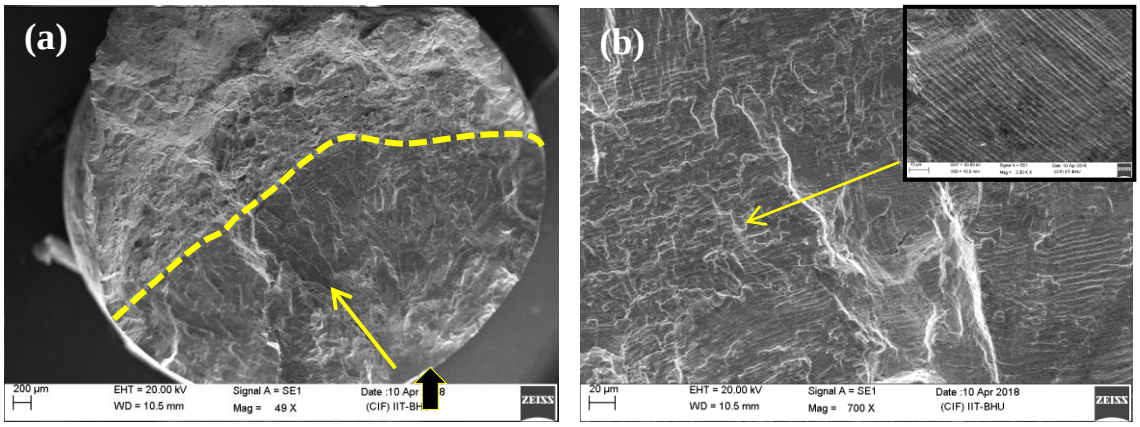

Fig. 5.25: SEM fractographs of the samples fatigue tested at 750^{o}C and at strain amplitude of ±0.20% showing: (a) crack initiation site (dark arrow) and growth direction (light arrow) and (b) striation morphology.

At this temperature, the largest portion of the life to propagate crack is in the direction perpendicular to the loading direction. It is evident that the inter-striation spacing is more as compared to that tested at room temperature. As a consequence, the fatigue life decreased with increase in temperature. At high strain amplitudes, at this temperature, the inter-striation spacing increased further. The inter-striation spacing was

found to increase with increase in strain amplitude. Inter-striation spacing was found to be 2-2.5 μm at ±0.2% strain amplitude and 8-10 μm at ±0.5% strain amplitude. The area of the fatigue crack growth zone consists nearly 40% of the area at ±0.2% and 25% at ±0.5%.

Figs. 5.27 and 5.28 shows fracture surfaces of the samples tested at 850^{o}C at strain amplitudes of ±0.2% and ±0.5% respectively. The multiple crack initiation sites are shown by thick arrows. The fracture behaviour is similar to that of observed at 750^{o}C except the increase in number of crack initiation sites and interstriation spacing. Interstriation spacing increased with increase in the strain amplitude. Inter-striation spacing was found to be 2-3.5 μm at ±0.2% strain amplitude and 11-13 μm at ±0.5% strain amplitude. The area of the fatigue crack growth zone was nearly 30% of the area at ±0.2% and 20% at ±0.5%.

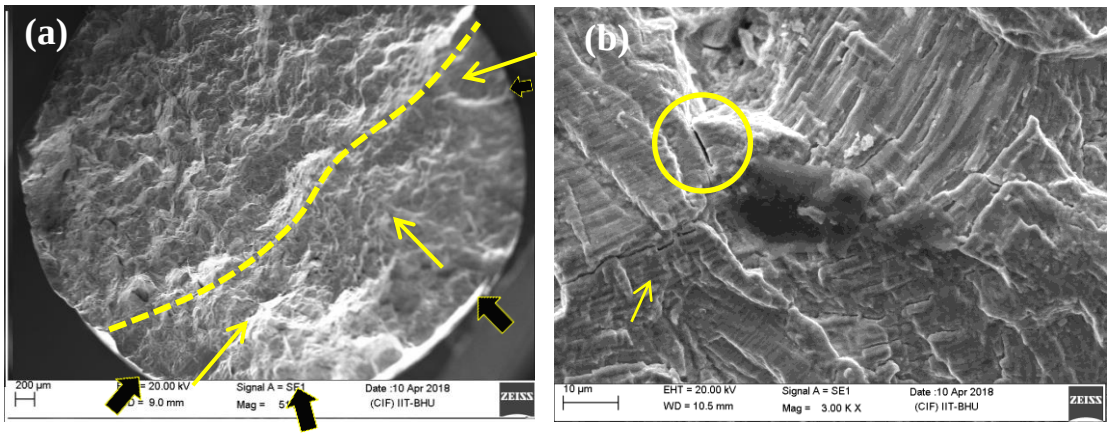

Fig. 5.26: SEM fractographs of the samples fatigue tested at 750^{o}C and at strain amplitude of ±0.50% showing: (a) multiple crack initiation sites as shown by dark arrow and light arrow indicates growth direction and (b) the striation morphology (arrow), and intergranular crack (circle).

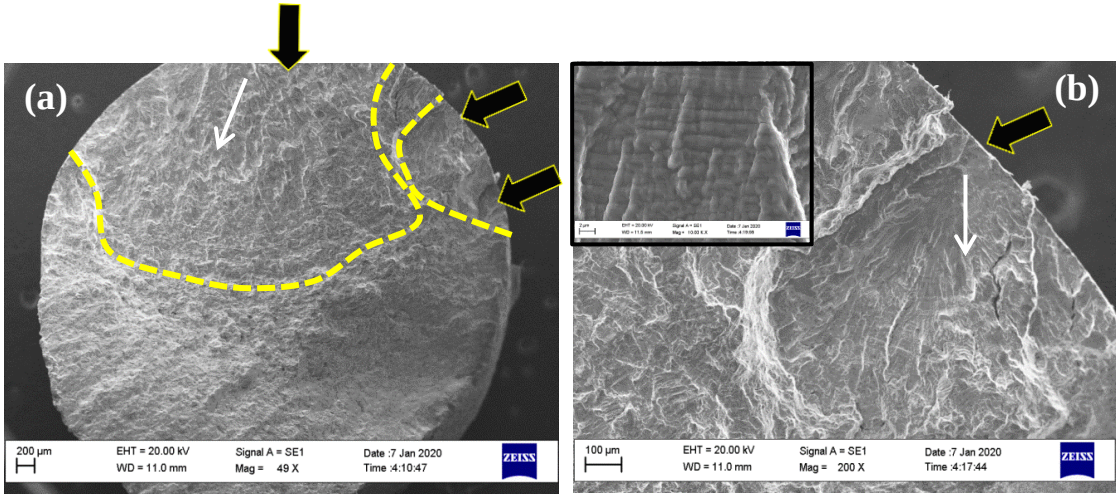

Fig. 5.27: SEM fractographs of the samples fatigue tested at 850^{o}C and at strain amplitude of ±0.20% showing: (a) multiple crack initiation sites as shown by dark arrow and (b) magnified view of the crack initiation site (arrow) and growth direction (light arrow) and the striation morphology.

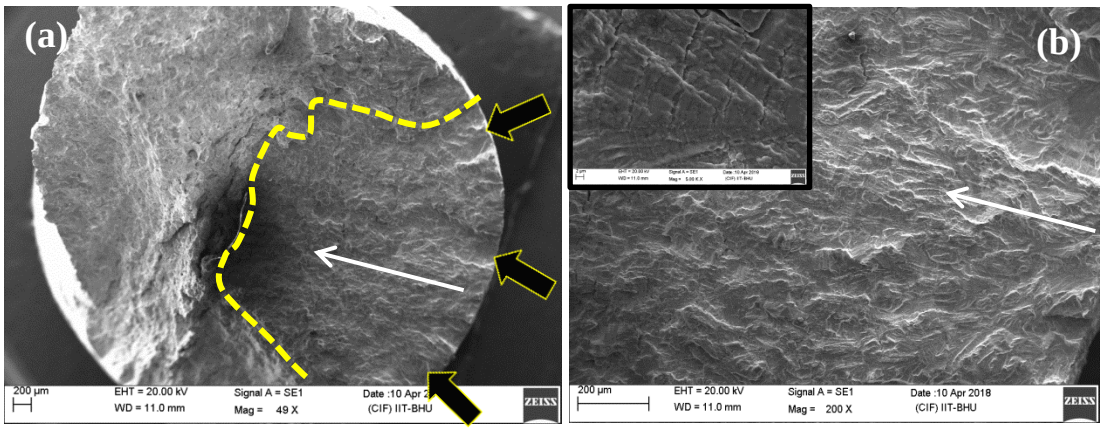

Fig. 5.28: SEM fractographs of the samples fatigue tested at 850^{o}C and at strain amplitude of ±0.50% showing: (a) multiple crack initiation sites as shown by dark arrow and light arrow indicates growth direction and (b) magnified view of the crack initiation site (arrow) and growth direction (light arrow) and the striation morphology.

Fig. 5.29 shows micrographs of the longitudinal cross section of the fatigue samples after fracture at ±0.5% strain amplitude at room temperature, clearly indicating the transgranular primary crack propagation (Fig. 5.29a). Bands of cavities along with carbides near the grain boundaries parallel to the loading direction are found throughout the structure (see dark arrow). Some carbide particles were found within the cavities

indicating formation of cavities during cyclic loading surrounding the carbide particle (Fig. 5.29b). Secondary transgranular cracks of very short length and intergranular cracks due to the presence of carbides are observed as shown in Fig. 5.29b. Undissolved precipitates in intergranular regions are shown in Fig. 5.29c.

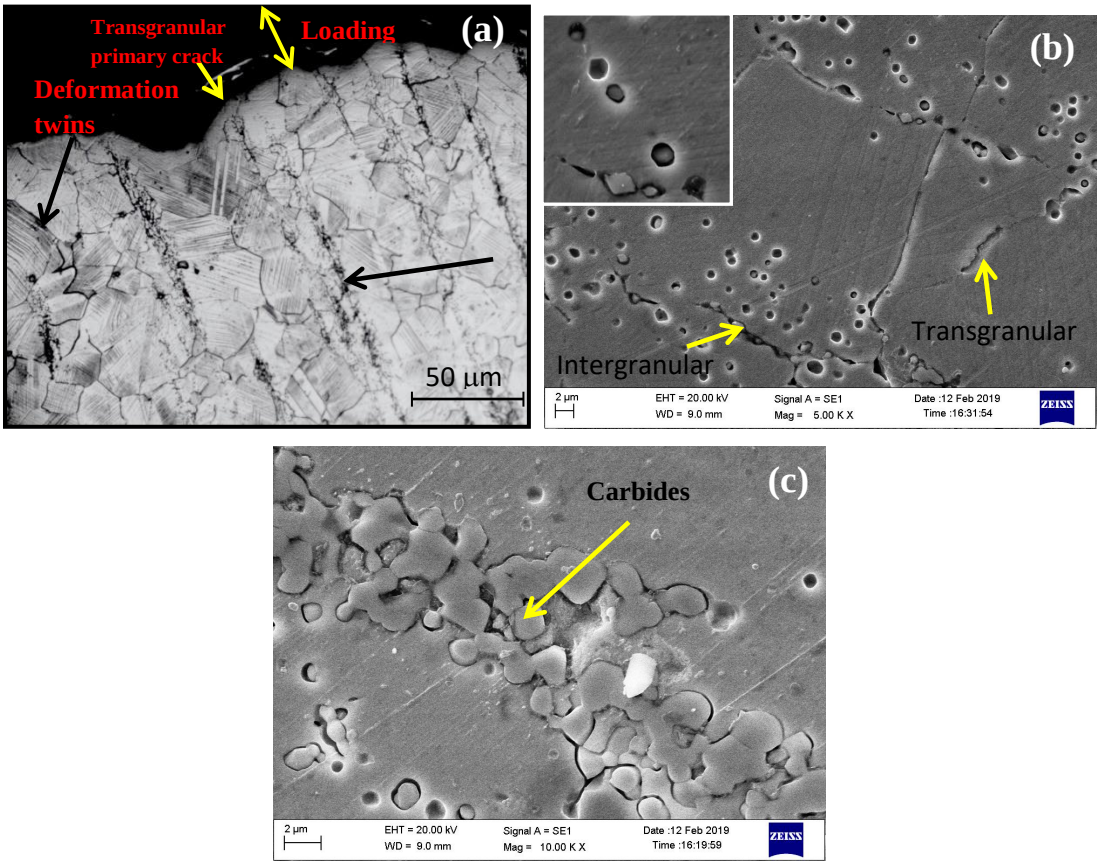

Fig. 5.29: Longitudinal cross section of the samples fatigue tested at RT and at strain amplitude of ±0.50%: (a) Optical micrograph showing transgranular primary crack and micro voids along with carbide particles aligned parallel to loading direction (dark arrow) (b) SEM micrograph of the micro voids shown in (a) along with carbide particles and also shows intergranular cracks due to presence of these carbides and (c) SEM micrograph showing cluster of carbide particles along grain boundary.

Fig.5.30 shows micrographs of the samples tested at 750^{o}C, the primary crack is transgranular but transformed to intergranular at some regions (Fig. 5.30a). Secondary crack initiation and propagation is in transgranular mode but at later stages it started propagating in intergranular mode as shown in Fig. 5.30b. Fig. 5.30c shows SEM micrograph of the multiple branches of secondary crack and change in direction of the

crack due to interaction with twins and carbide particles apart from grain boundaries. Fig. 5.30d shows the change in direction of secondary crack due to Ti(C, N) particle interaction. Fig.5.31 shows micrographs of the samples tested at 850^{o}C, which indicates the primary crack is transgranular but also propagated in transgranular mode (Fig. 5.31a). No evidence of intergranular cracks can be seen in this condition. Fig. 5.31c shows the formation of fine grains which indicates recrystallization of grains occurs at this temperature. Other features were similar to that observed at 750^{o}C.

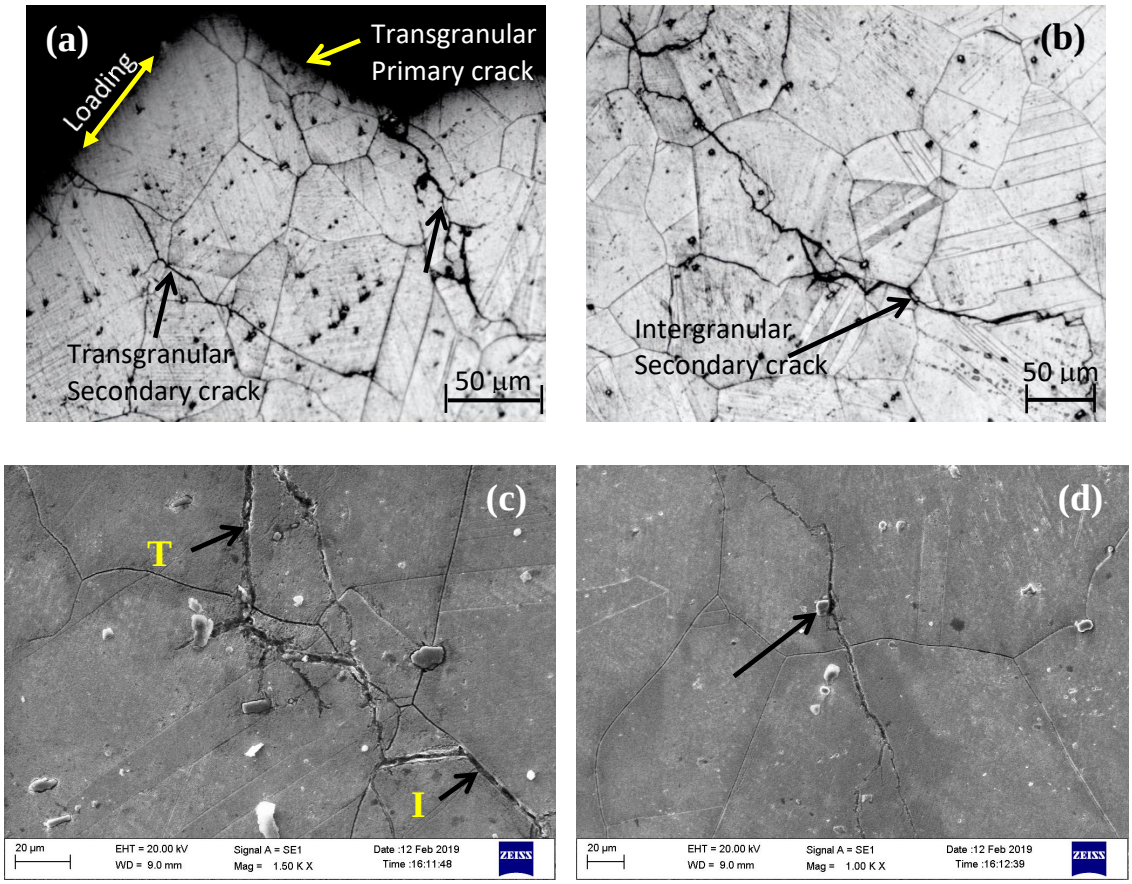

Fig. 5.30: Longitudinal cross section for the samples fatigue tested at 750^{o}C and at strain amplitude of ±0.50% (a) Optical micrographs showing primary transgranular crack and multiple secondary transgranular cracks, (b) Secondary transgranular crack (T) propagation converting to intergranular (I) (c) SEM micrograph of the magnified view of (b) and (d) SEM micrograph showing change in crack direction due to Ti(C,N) particles interaction.

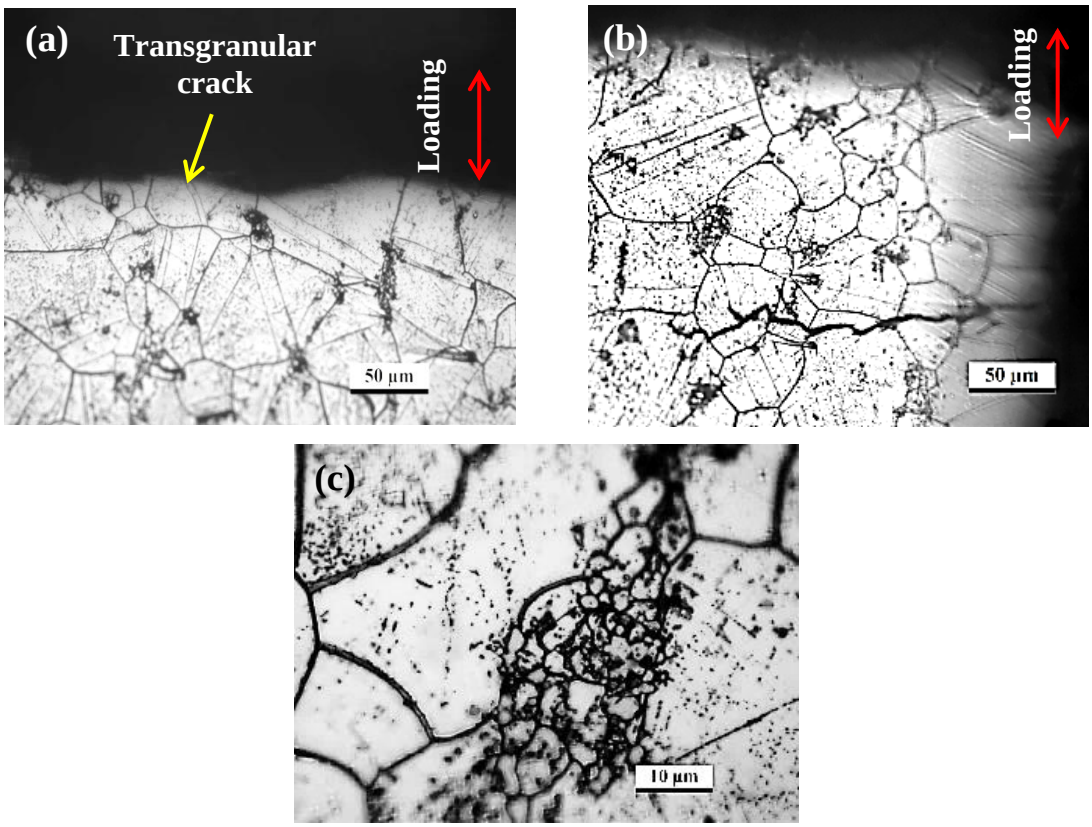

Fig. 5.31: Longitudinal cross section for the samples fatigue tested at 850^{o}C and at strain amplitude of ±0.50% (a) Optical micrographs showing primary transgranular crack at the fracture end (b) transgranular crack propagation (c) formation of fine grains through recrystallization of grains.

5.13 Discussion

5.13.1 Cyclic Stress Response and Cyclic Stress-Strain Behaviour

The cyclic stress-strain diagram shows that this alloy exhibits cyclic hardening at RT, 750^{o}C and 850^{o}C at all the strain amplitudes studied. In cyclic deformation, materials tend to harden or soften until they reach a saturation stress. Cyclic hardening in the initial cycles is due to the dislocation multiplication and accumulation within the grains. Multiplication of twins and formation of deformation twins at the lower strain amplitude is prime deformation mechanism at lower strain amplitude. The poorly developed cells may be the result of dislocations from different slip systems interacting and locking each other at intersected regions. The initial higher hardening rate with

increase in strain amplitude, at the room temperature (Fig. 5.2a), may be attributed to higher degree of multiplication of dislocations within the slip bands which contribute to most of the deformation [127]. During plastic deformation, primarily there is dislocation-dislocation interaction and dislocation-precipitate interaction which cause strain hardening in these alloys. In the present case, dislocation structure is highly heterogeneous at low strain amplitudes whereas well defined dislocation pairs are found at high strain amplitudes. The carbide particles earlier present along the grain boundaries, formed as lamella and needle like particles during cyclic loading. Continuous cyclic hardening observed at the 750^{o}C can be attributed to the formation of dislocation substructure which provides numerous sites for heterogeneous precipitation of fine $M_{23}C_6$ particles. The precipitates in turn, stabilize the substructure during further cycling, preventing the recovery processes [57]. The high volume fraction of precipitate particles is responsible for the higher rate of work hardening even in tensile loading. Though the yield strength of this alloy is low, there is a steep rise in cyclic hardening after stabilisation. The two-slope behaviour observed in hardening at 750^{o}C (Fig. 5.2b), can be associated with the precipitation of γ' and carbides, that takes place only after certain number of cycles and plastic strain accumulation. The rate of cyclic hardening increased rapidly with increase in the volume fraction of precipitates, prime contribution is from γ'. Increase in hardening (Table 5.3) with increase in strain amplitude is due to increase in the dislocation density and mutual interaction of dislocations as well as with the precipitates. In addition DSA at 750^{o}C also adds to steep cyclic hardening [128].

The carbides formed at 850^{o}C are bigger in size compared to that at 750^{o}C and they are less in number and are inhomogeneous which caused reduction in degree of hardening. The prime reason for decrease in degree of hardening again at higher strain

amplitude compared to lower strain amplitude at elevated temperature (Fig. 5.4a), is due to the difference in volume fraction of precipitates that caused less dislocation precipitate interaction. Figs. 5.17-5.20 clearly shows that the volume fraction of precipitates is more at the lower strain amplitude compared with that at higher strain amplitude because of longer duration of exposure at the elevated temperature. Monotonic tensile stress strain curve lies below the cyclic stress strain curve for all the three temperatures indicating cycling hardening for the reasons discussed in the deformation behaviour section (5.13.2). This behaviour is in line with the hypothesis that cyclic hardening is expected in the materials with S_{UTS}/ S_{YS} greater than 1.4 (Table 5.1) and monotonic strain hardening exponents (n) values greater than 0.15 (Table 5.1) [109, 129]. Non-Masing behaviour is generally associated with localized deformation whereas Masing behaviour is observed with homogeneous deformation. Non-Masing behaviour of this material may be attributed to change in dislocation configuration and localised deformation with multiple cross slip activation.

The plastic strain amplitude–number of reversals to failure ($2N_f$) plot for this alloy (Fig. 5.8d) illustrates that for the same applied strain amplitude, fatigue life is higher at room temperature as compared with those at high temperatures. Similar trend has been observed in earlier studies as well [59-63, 130-132]. The cyclic stress strain curves are generally determined from the cyclically stabilised hysteresis loops. This criterion fails in some cases where the stress is not stabilised and there is continuous hardening in the alloy. In that case strain energy life relationship gives best approximation as the plastic strain energy saturates in the early stage of fatigue [118]. Both strain energy based relationship and strain life relationship show almost the same result because both the criteria are based on plastic strain. The results in the present investigation indicate that both the plastic strain energy–life as well as plastic strain–life

relationship are in good approximation at room temperature but with first one is found more accurate, but there is much variation in the predicted life at higher temperatures due to change in precipitation kinetics and non-Masing behaviour of this material, plastic strain-life relation is in good agreement. The various fatigue parameters determined in this investigation are in good agreement with the previous published values for the same alloy [130-132] though there was slight variation in test parameters and material condition.

5.13.2 Deformation Behaviour under Cyclic Loading

At lower strain amplitudes the rate of hardening is low, at room temperature, though no softening is observed after stabilisation. Micro twins are initiated when easy dislocation glide is hindered and they contribute to most of the localised deformation. The hindrance to easy glide can be inferred from the presence of dislocations outside the twins as in Fig. 5.13b. The main deformation process at this strain amplitude is through slip. With increase in strain amplitude very high rate of initial hardening is observed room temperature, due to more dislocation-dislocation interaction at the high strains. After saturation stage again softening is observed until failure. This trend indicates dislocation multiplication (Fig. 5.14b) and accumulation within the initiated slip band during the regime of hardening. Samples of the interrupted fatigue tests carried out at this strain amplitude, to explore the prime cause of hardening in the initial 80 cycles, show alignment of dislocations in slip bands in straight lines and the deformation mechanism to be slip. The slip was restricted to one system parallel to {111} planes. Upon continuation of cyclic loading further, rate of annihilation of dislocations increases due to increased dislocation density and reaches to saturation state. During softening stage at 1500 cycles, dislocation substructure develops with

more number of slip bands and low density of dislocations but also there were cross slip bands due to activation of another variant of the same family with more uniform distribution. At high strain amplitude the cellular dislocation structures or sub grains were fully developed and densely clustered. During cyclic deformation, mutual interaction of dislocations with precipitates, grain boundaries etc. increase the resistance to plastic deformation that takes place and causes cyclic hardening. This is prime cause of increase in the rate of cyclic hardening at 750^{o}C compared to that at room temperature. The precipitation kinetics is accelerated due to the enhanced diffusion of carbide forming elements along dislocations and numerous vacancies generated during cyclic deformation. At 750^{o}C uniformly distributed fine precipitates are formed. It is assumed that the precipitation of fine carbides is due to the fact that the number of dislocations is drastically increased by the superimposed cyclic loading, the dislocation tangles so formed serve as heterogeneous sites for precipitation.

Rao et al. [57] studied this alloy at 750^{o}C and 850^{o}C, and claimed that dislocations, dislocation tangles and planar slip bands act as preferential sites for nucleation of $M_{23}C_6$ precipitates. The occurrence of γ' particles at 750^{o}C in the present investigation is in line with the earlier observations following thermal aging studies made by Wu et al. [15] and Kirchhöfer et al. [14]. Pan et al. [133] observed γ' particles in this alloy following thermal fatigue tests conducted even at 600^{o}C. At 850^{o}C the reduction in number precipitates, their inhomogeneous distribution, the absence of γ' particles reduced the hardening rate. The absence of γ' particles at 850^{o}C is also mentioned by Mankins et al. [12]. During monotonic loading also, the degree of work hardening and strain hardening exponent are very high at this temperature for this alloy. Accumulation of dislocations during interaction with precipitates caused more hardening at 850^{o}C compared to that at RT at the identical strain amplitudes. The

decrease in fatigue life at the higher strain amplitude resulted partially from decrease in the plastic strain amplitude and consequent increase in the stress amplitude. At the high level of stress amplitude, the critical size of crack required for final fracture is less and hence fatigue life reduces.

5.13.3 Fracture Behaviour

The strain amplitude and temperature influence stage I crack initiation and stage II crack propagation to a great extent. Increase in temperature increases the number of crack initiation sites from single to multiple sites. The stage II crack propagation dominates the largest portion of the fracture surface exhibiting striations on the fracture surface. The slip bands which form due to cyclic loading contain extrusions and intrusions and lead to the production of point defects, which then develop into micro cracks and coalesce to form macro cracks. At room temperature, the presence of precipitates near the grain boundary regions causes micro voids to nucleate at the particle matrix interfaces and grow in size under the stress field of advancing crack and cyclic loading. These micro voids or cavities are generally formed at the precipitate regions at high temperature. At higher strain amplitudes, stress concentration at some of the grain boundaries arising from the higher applied strain exceeds the rupture stress of the grain boundary and leads to intergranular cracking in some regions at higher temperatures. This indicates mixed mode type of fracture. Sudden drop in stress amplitude prior to failure is mainly attributed to fast growth and coalescence of cracks. In the present case, the fracture mode was ductile at both the strain amplitudes at room temperature but at higher strain amplitudes at 750^{o}C, general brittle mode of fracture was observed indicating the dependence of deformation mode on strain amplitude. Ridges or ratchet marks originate when multiple cracks are nucleated at different planes

or heights in gage section of the sample and leads to formation of vertical step on the fracture surface. Once the initial lines link together, the ratchet lines disappear. Therefore, the number of ratchet marks is a good indication of the number of nucleation sites and associated ratchet lines [117]. In normal scenario, a large fatigue life is spent in crack nucleation in stage I at lower strain amplitudes compared to higher strain amplitudes and crack propagation is vice versa [118]. Thus, the decrease in fracture area with increase in strain amplitude from ±0.2% to ±0.5% was observed in the present alloy. The smaller area of fatigue fracture at the higher strain amplitudes was due to the more inter striation spacing as compared to that at lower strain amplitude, due to high cyclic stress response and less number of cycles can be accommodated in the area. Prominent faceted features were observed at higher strain amplitudes and temperatures without striation marks (Fig. 5.26b), due to formation of fine carbide precipitates interacting with the dislocations and higher work hardening rate of this alloy at 750^{o}C [57, 64]. The absence of saturation stage in the cyclic stress response curve at elevated temperatures (Figs. 5.2b and c), and the early onset of the stress drop may be due to the reduced capacity to work harden further in the presence of the intergranular cracks shown in Fig. 5.30c.

The formation of cavities along grain boundaries and near the grain boundaries (Fig. 5.29b) may be attributed to intersection of slip bands with grain boundaries or carbide particles in the grain boundary as observed earlier [134, 135]. Cavity formation may also result from the coalescence of dislocations at the head of a pile up against the grain boundary [136]. These cavities form generally at interface between carbide and metal especially where there is a discontinuity in the grain boundary. The extent of cavitation on a boundary is dependent mainly on its orientation with respect to stress axis and generally occurs on those boundaries which lie roughly parallel to the direction

of maximum principal stress. Dyson et al. [134] and Saegusa et al. [135] reported this for nickel base alloys on pre-straining or deformation at room temperature.

5.14 Chapter Summary

The results of detailed investigation on the low cycle fatigue behaviour of the Inconel 617 alloy at three test temperatures (RT, 750^{o}C and 850^{o}C) and the corresponding deformation and fracture studies can be summarized as given below.

1. Inconel 617 alloy showed initial cyclic hardening at room temperature before saturation at lower strain amplitudes, due to pile ups of planar array of dislocations within the slip bands and their interaction with each other and with stacking faults. At strain amplitude of ± 0.5%, the alloy showed cyclic softening caused by cross slip and formation of cell structure after very high rate of initial hardening.
2. At 750^{o}C, the alloy showed continuous cyclic hardening and the rate of hardening was high at 750^{o}C for all the strain amplitudes compared to that at room temperature and 850^{o}C. Two slope behaviour of cyclic hardening was observed due to precipitation of fine γ' and carbide particles after certain number of cycles.
3. The plastic strain amplitude increased with increase in temperature at all the strain amplitudes studied. The cyclic stress strain curves, developed from hysteresis loops at half-life were above the monotonic stress strain curve at three temperatures depicting the cyclic hardening behaviour of the material.
4. Non-Masing behaviour was observed for the alloy at RT, 750^{o}C and 850^{o}C.
5. The fatigue life decreased with increase in temperature and strain amplitude. Coffin Manson relationship was followed at all the three temperatures studied.

6. Continuous decrease in dislocation density was observed with increase in temperature and strain amplitude. Fine carbide and γ′ precipitates were formed at 750^{o}C and hardening was increased and fatigue life was decreased. γ′ precipitates were not observed at 850^{o}C.
7. Inter-striation spacing increased with increase in temperature and strain amplitude. Number of secondary cracks increased with increase in temperature.